ISTANBUL TECHNICAL UNIVERSITY ★ GRADUATE SCHOOL

EFFECT OF DYNAMIC CONTACT ANGLE MODELS ON THE DROPLET SPREAD SIMULATIONS

M.Sc. THESIS

Tahir Tekin FİLİZ

Department of Mechanical Engineering

Heat - Fluids Programme

JANUARY 2022

ISTANBUL TECHNICAL UNIVERSITY ★ GRADUATE SCHOOL

EFFECT OF DYNAMIC CONTACT ANGLE MODELS ON THE DROPLET SPREAD SIMULATIONS

M.Sc. THESIS

Tahir Tekin FİLİZ
(503171129)

Department of Mechanical Engineering

Heat - Fluids Programme

Thesis Advisor: Prof. Dr. İlyas Bedii ÖZDEMİR

JANUARY 2022

İSTANBUL TEKNİK ÜNİVERSİTESİ ★ LİSANSÜSTÜ EĞİTİM ENSTİTÜSÜ

DİNAMİK TEMAS AÇISI MODELLERİNİN DAMLACIK YAYILMASI BENZETİMLERİNE ETKİSİ

YüKSEK LİSANS TEZİ

Tahir Tekin FİLİZ
(503171129)

Makine Mühendisliği Anabilim Dalı

Isı Akışkan Programı

Tez Danışmanı: Prof. Dr. İlyas Bedii ÖZDEMİR

OCAK 2022

Tahir Tekin FİLİZ, a M.Sc. student of ITU Graduate School student ID 503171129, successfully defended the thesis entitled "EFFECT OF DYNAMIC CONTACT ANGLE MODELS ON THE DROPLET SPREAD SIMULATIONS", which he prepared after fulfilling the requirements specified in the associated legislations, before the jury whose signatures are below.

Thesis Advisor :	**Prof. Dr. İlyas Bedii ÖZDEMİR** Istanbul Technical University	.....
Jury Members :	**Prof. Dr. Cem PARMAKSIZOĞLU** İstanbul Technical University	.....
	Doç. Dr. İlyas YILMAZ İstanbul Bilgi University	.....

Date of Submission : 11 January 2022
Date of Defense : 18 January 2022

FOREWORD

I would like to thank my advisor Prof. Dr. İ. Bedii Özdemir for all the support and knowledge he has provided me, and my wife Elifsu Filiz for always being there for me.

January 2022

Tahir Tekin FİLİZ
(B.Sc.)

TABLE OF CONTENTS

Page

ABBREVIATIONS

CFD	**:** Computational Fluid Dynamics
CFL	**:** Courant–Friedrichs–Lewy
DCA	**:** Dynamic Contact Angle
MSDE	**:** Maximum Spread Diameter Error
MSFE	**:** Mean Spread Factor Error
MULES	**:** Multidimensional Universal Limiter for Explicit Solution
PISO	**:** Pressure Implicit with Splitting of Operator
VOF	**:** Volume of Fluid

SYMBOLS

A	: Area
Ca	: Capillary Number
C_α	: Compression Coefficient
D	: Diameter of The Droplet
D_0	: Initial Diameter of The Droplet
F	: Shift Factor
f_{hoff}	: Hoffman Function
F_σ	: Surface Tension Force
$\vec{g}$	: External Volume Force
H	: Contact Angle Hysteresis
m	: Mass
$\dot{m}$	: Mass Flow
$\vec{n}$	: Normal vector
P	: Pressure
P_1, P_2, P_k	: Pressure of Phase 1, 2, k
Re	: Reynolds Number
S_f	: Face Area Vector
t	: Time
T	: Stress Tensor
T_1, T_2, T_k	: Stress Tensor of Phase 1, 2, k
$\vec{u}$	: Velocity
$\vec{u}_1, \vec{u}_2, \vec{u}_k$	: Velocity of Phase 1, 2, k
u_{cl}	: Contact Line Velocity
u_r	: Relative Velocity
U_0	: Initial Velocity of The Droplet
V	: Volume
V_k	: Volume Occupied by Phase k
We	: Weber Number
$\vec{x}$	: Position Vector
α	: Volume Fraction
$\alpha_1, \alpha_2, \alpha_k$	: Volume Fraction of Phase 1, 2, k
β	: Any Flow Variable
Γ	: Flow Domain Boundary
$\Gamma_1, \Gamma_2, \Gamma_k$	: Flow Domain Boundary of Phase 1, 2, k
Γ_f	: Phase Interface
θ_A	: Advancing contact angle
θ_D	: Dynamic contact angle
θ_E	: Equilibrium contact angle
θ_R	: Receding contact angle
κ	: Curvature of the Phase Interface
μ	: Dynamic Viscosity

μ_1, μ_2, μ_k : Dynamic Viscosity of Phase 1, 2, k
μ_l : Dynamic Viscosity of the Liquid Phase
ρ : Density
ρ_1, ρ_2, ρ_k : Density of Phase 1, 2, k
ρ_l : Density of the Liquid Phase
σ : Surface Tension Coefficient
σ_{LG} : Surface Tension Coefficient Between Liquid and Gas
σ_{SG} : Surface Tension Coefficient Between Solid and Gas
σ_{SL} : Surface Tension Coefficient Between Solid and Liquid
τ : Dimensionless Time
Φ : Face Flux
Ω : Open Flow Domain
$\overline{\Omega}$: Closed Flow Domain
$\Omega_1, \Omega_2, \Omega_k$: Open Flow Domain of Phase 1, 2, k
$\overline{\Omega}_1, \overline{\Omega}_2, \overline{\Omega}_k$: Closed Flow Domain of Phase 1, 2, k
$\mathbb{1}$: Phase Indicator Function
$\mathbb{1}_1, \mathbb{1}_2, \mathbb{1}_k$: Phase Indicator Function of Phase 1, 2, k

LIST OF TABLES

Page

LIST OF FIGURES

Page

EFFECT OF
DYNAMIC CONTACT ANGLE MODELS
ON THE DROPLET SPREAD SIMULATIONS

SUMMARY

Many industrial processes such as inkjet printing, spray coating and spray cooling, involve the liquid droplets impacting onto solid surfaces. Hence, an accurate estimation of the impact of a droplet onto a solid surface is of great importance because unexpected behaviors of droplets may result in bad quality products or services. In order to make an accurate numerical simulation, one needs to solve many challenging problems such as interface localization and the estimation of dynamic contact angle (DCA). There are many techniques developed for the localization of the phase interface in two phase flows. The most popular techniques are the level set, the volume of fluid (VOF) and the Lagrangian methods. The Lagrangian methods are computationally expensive, and the level set method is not mass conservative. Therefore, in this work we have selected the VOF method and conducted our simulations using two different interface capturing schemes, an algebraic algorithm named Multidimensional Universal Limiter for Explicit Solution and a geometrical algorithm named IsoAdvector. We have compared four DCA models, the Quasi-Dynamic, the Shikhmurzaev, the Kistler and the Bracke models. We have used OpenFOAM, an open source computational fluid dynamics (CFD) software as our computation platform. We have implemented the DCA models and used them as a boundary condition for the phase fraction equation, which is used by the VOF method in order to locate the phase interface. Numerical simulations were compared with five different experimental results. The performances of the simulations were evaluated using two metrics, the mean spread factor error and the maximum spread diameter error. Even though the performances of the DCA models are similar, for higher Reynolds numbers, the Shikhmurzaev model gave the most accurate results, whereas the Kistler model and the Quasi-Dynamic model gave better estimations in low Reynolds numbers. We've also concluded that the IsoAdvector scheme is not suitable for the droplet impact simulations with low Weber numbers.

DİNAMİK TEMAS AÇISI MODELLERİNİN DAMLACIK YAYILMASI BENZETİMLERİNE ETKİSİ

ÖZET

Sıvı damlacıklarının katı bir yüzeye çarpması; mürekkep püskürtmeli baskı, sprey kaplama, püskürtmeli soğutma, tarım ilaçlarının uygulanması gibi birçok endüstriyel işlemin etkili olarak gerçekleştirilmesinde büyük önem taşır. Örneğin, sprey kaplama işleminde hava baloncuğu oluşumu ürünün kalitesini düşürmekle beraber, eğer damlacıkların davranışları modellenebilirse ortadan kaldırılabilecek bir sorundur. Diğer bir örnek ise, hem kağıda yazdırma işlemlerinde, hem de organik ışık yayan diyot (OLED) panellerinin üretiminde kullanılan mürekkep püskürtmeli yazdırma işlemi, damlacıkların ıslattığı alandan direkt olarak etkilenmektedir. Bu nedenle, bir damlacığın katı bir yüzey üzerindeki davranışının doğru bir şekilde tahmin edilmesi, endüstriyel ürünlerin kalitesinin artmasına olanak sağlayacaktır. Bu süreçlerin iyileştirilmesi için yapılan fiziksel deneyler meşakkatli ve pahalı olduğu için, damlacıkların sayısal benzetiminin yapılması sıklıkla tercih edilen bir yöntemdir.

Bir sıvı damlasının katı bir yüzey üzerinde yayılması viskoz, atalet ve temas hattı kuvvetlerinin etkisi altında gerçekleşen, oldukça dinamik ve karmaşık bir olaydır. Yayılım olayını etkileyen birçok faktör bulunmaktadır. Bunlardan bazıları damlacığın katı yüzeye çarpma anındaki çapı ve hızı, yüzey pürüzlülüğü, basınç, viskozite, katı yüzeyinin ıslanabilirliği, Reynolds sayısı ve Weber sayısı olarak sıralanabilir. Reynolds sayısı atalet kuvvetlerinin viskoz kuvvetlere oranı, Weber sayısı ise atalet kuvvetlerini yüzey gerilimine oranı olarak tanımlanır.

Yukarıda bahsi geçen sebeplerden ötürü bir damlacığın sayısal benzetiminin yapılması oldukça zor bir süreçtir ve çözülmesi gereken bir çok problem barındırır. Bu problemlerden bazıları faz ara yüzeyinin yakalanması/izlenmesi, dinamik temas açısının tespiti, yüzey gerilmesinin modellenmesi ve temas hattı hızının belirlenmesi olarak sıralanabilir.

İki fazlı akışlarda faz arayüzünün lokalizasyonu için geliştirilmiş birçok teknik vardır. En popüler teknikler seviye kümesi (level set), akışkan hacmi (volume of fluid, VOF) yöntemi ve Lagrange yöntemleridir. Lagrange yöntemleri kullanılarak yapılan benzetimler diğer yöntemlere kıyasla oldukça yüksek bir hesaplama gücü gerektirir ve seviye kümesi yönteminde kütle kaybı (hesaplama süresi ilerledikçe sıvı kütlesinin gaz kütlesine dönüşmesi) sorunları mevcuttur. Bu sebeplerden ötürü bu çalışmada yapılan sayısal benzetimlerde VOF metodu kullanılmıştır.

VOF yönteminde farklı akışkan fazları hacim kesri (volume fraction) fonksiyonu ile takip edilir. Hacim kesri, bir hesaplama hücresinde bulunan akışkanın kompozisyonunu belirten bir fonksiyondur. Örneğin bir hücre tamamen bir akışkan

ile doluysa, hacim kesri fonksiyonu 1 değerini alır, eğer ki o hücrede o akışkan mevcut değilse 0 değerini alır. Dolayısıyla, hacim kesri fonksiyonunun 0 ile 1 arasında olması, hücrede akışkan ara yüzeyi varlığını göstermektedir. Her bir zaman aralığında hacim kesri denklemi de korunum denklemleriyle birlikte çözülüp ara yüzeyin adveksiyonu sağlanır.

Faz ara yüzeyinin keskin olmasını sağlamak için özel ayrıklaştırma yöntemlerinin kullanılması gerekir. OpenFOAM'da kullanılan standart metot, cebirsel bir metot olan Multidimensional Universal Limiter for Explicit Solution (MULES) metodudur. Ancak MULES metodu kullanıldığında ara yüzey birkaç hesaplama hücresine yayılır. Bu problemi ortadan kaldırmak için, geometrik bir metot olan IsoAdvector metodu önerilmiştir. Bu çalışmada hem MULES hem de IsoAdvector metotları kullanılarak sayısal benzetimler yapılmıştır.

Damlacıkların sayısal benzetiminin isabetliliğini etkileyen bir diğer faktör ise temas açısının modellenmesidir. Temas açısı, iki karışmaz akışkanın duvarla temas ettiği noktada duvar ile akışkan ara yüzeyi teğetinin yaptığı açıdır. Akışkanların hareketsiz olduğu durumda, bu açı akışkan-duvar sisteminin bir özeliğidir, ve bu durumda temas açısı, denge temas açısı olarak adlandırılır.

Akışkanların hareket ettiği durumda ise temas açısı yalnızca akışkan-duvar sistemine değil aynı zamanda akışa da bağlıdır ve dinamik temas açısı olarak adlandırılır. Hareketli durumda gözlemlenen dinamik temas açısının davranışı henüz tam olarak anlaşılamamış olsa da geçtiğimiz on yıllarda araştırmacılar pek çok dinamik temas açısı modeli geliştirmişlerdir. Pek çok dinamik temas açısı modeli, dinamik temas açısını temas hattı hızının ve kapiler sayısının bir fonksiyonu olarak ifade eder.

Bu çalışmada; Shikhmurzaev, Kistler ve Bracke dinamik temas açısı modellerini ve Sanki-Dinamik temas açısı modeli kullanılarak, literatürde bulunan beş farklı damlacık çarpması deneyinin sayısal benzetimleri yapılmıştır. Deneylerin Weber sayıları 1.81 ile 93 aralığında, Reynolds sayıları ise 36 ile 4010 aralığındadır. Hesaplama platformu olarak açık kaynaklı bir hesaplamalı akışkanlar dinamiği yazılımı olan OpenFOAM programı kullanılmıştır. Her bir dinamik temas açısı modeli faz kesri denklemine bir sınır şartı olarak verilmiştir. Benzetimlerin performanslarını değerlendirmek için ortalama yayılma faktörü hatası ve maksimum yayılma çapı hatası ölçütleri kullanılmıştır.

Sonuçta tüm dinamik temas açısı modellerinin deneylerle uyumlu sonuçlar verdiği gözlemlenmiştir. Tüm benzetimlerden elde edilen ortalama yayılma faktörü hatası en düşük %1.34, en yüksek %11.33 olarak bulunmuştur. Benzer olarak, maksimum yayılma çapı hatası %1.24 ile %11.31 aralığında bulunmuştur.

Düşük Reynolds sayısına sahip deneylerde, benzetimlerin maksimum yayılma çapını deneysel sonuçlara oranla daha düşük tahmin ettiği görülmüştür. Yüksek Reynolds sayısına sahip deneylerde ise maksimum yayılma çapı gerçekte olduğundan daha yüksek bulunmuştur.

Dinamik temas açısı modellerinin performansları benzer olsa da yüksek Reynolds sayılarında Shikhmurzaev modeli en doğru sonuçları verirken, Kistler modeli ve Sanki-Dinamik model düşük Reynolds sayılarında daha iyi tahminler vermiştir.

Ayrıca, IsoAdvector'ın düşük Weber sayılarına sahip damlacık etkisi simülasyonları için uygun olmadığı görülmüştür.

Bu çalışmanın ilk bölümünde damlacık çarpması olayı, bu olaya etki eden faktörler ve literatürde damlacık çarpması benzetimlerinde kullanılan farklı yöntemlerden bahsedilmiştir. Çalışmanın ikinci bölümü iki fazlı akış denklemlerinin türetilmesine adanmıştır. Üçüncü bölümde önceki bölümde elde edilen denklemler kullanılarak elde edilen VOF metodu formülasyonu ayrıntılı olarak incelenmiştir. Dördüncü bölümde temas açısı kavramı açıklanmış ve bu tezde kullanılan dinamik temas açısı modelleri tanıtılmıştır. Beşinci bölümde benzetimi yapılan deneyler ve benzetim ortamı tanıtılmıştır. Altıncı bölümde benzetim sonuçları verilmiş ve sonuçlara dayalı bulgular tartışılmıştır. Son bölümde ise çalışmadan elde edilen genel sonuçlar verilmiştir.

1. INTRODUCTION

Many industrial processes and products such as inkjet printing, spray cooling, trickle bed reactors, fuel injection and spray painting [2–4], involve liquid droplets impacting onto a solid surface. It is important to estimate the outcomes of the wetting because it has a significant impact on the quality of the products of these industrial processes. For instance, in inkjet printing, which is not only used for printing on paper, but also used in the organic light-emitting diode (OLED) technology [2], an accurate estimation of the area wetted by the droplet is of crucial importance. Another example is droplet splashing in spray painting, where it is aimed to avoid air entrainment as much as possible [5]. Generally, the experiments conducted to improve these procedures are time consuming and expensive. An alternative to the tedious trial and error procedures is numerical simulations.

Spreading of a droplet is highly dynamic and complex phenomenon which is governed by viscous, inertial and contact line forces. It is affected by many factors such as initial droplet diameter and velocity, surface roughness, pressure, viscosity and wettability [6]. Wettability, as the name suggests, is the measure of a liquid's ability to wet the solid surface [7] and it is a result of the balance between adhesive and cohesive forces [8]. Wettability is quantified by the equilibrium contact angle, θ_E, which is the angle between the surface of the solid and the free surface of the liquid. Low θ_E corresponds to higher wettability and, similarly, high θ_E corresponds to lower wettability as shown in Figure 1.1. If the contact angle is greater than 90° the surface is said to be hydrophobic, and if the contact angle is less than 90° the surface is said to be hydrophilic [9]. The equilibrium contact angle, θ_E, is a thermodynamic property of the liquid-gas-solid system [10]. However, when the contact line, which is the intersection of the liquid's free surface and the surface of the solid, is in motion, the system is no longer in an equilibrium state and the contact angle diverges from θ_E. In such cases the angle between the surface of the solid and the free surface of the liquid is called the dynamic contact angle (DCA).

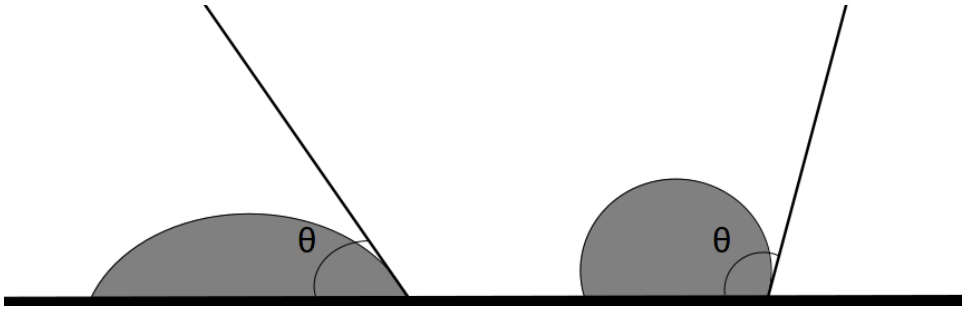

Figure 1.1 : Hydrophobic and hydrophilic surfaces.

There are many challenging factors in the numerical simulation of droplet spreading, such as localization of the phase interface, determining the contact line velocity and estimation of the contact angle. The methods proposed to solve these problems are introduced below.

There are two groups of interface localization techniques that are widely employed in flow problems with moving interfaces, namely interface tracking and interface capturing methods. Interface tracking methods are used in numerical simulation of droplet impact by many researchers [11–16]. In the interface tracking methods Lagrangian marker particles are used to track the interface explicitly. This explicit tracking of the interface can be very accurate since a large number of particles can be used, and since the interface is accurately estimated, the errors regarding surface tension are reduced [3]. However, these methods have issues with handling topological changes such as bubble entrapment or break up of droplets due to the construction of the interface by interpolating the Lagrangian marker particles [3]. Besides, due to the high number of particles, Lagrangian techniques are computationally expensive.

In the interface capturing methods, the interface is given implicitly by an auxiliary function. Two of the widely used interface capturing techniques in the droplet spread are the volume of fluid method (VOF) [4, 17–23] and the level set method [24–27]. These methods are popular among researchers because of their low computational cost. The VOF method locates the interface using the volume fraction function where a value of unity or zero indicates the presence or absence of a phase, respectively, and the values between 1 and 0 indicates the presence of the interface. In the level set method the interface is located using a signed distance function: Negative and positive values of this function distinguish the fluids, and zero level set indicates the boundary between fluids. The advantage of the VOF method over the level set method is while the mass

cannot be conserved in the level set method, in the VOF method it can. On the other hand, the VOF method is more prone to creating spurious currents compared to level set method. A schematic representation of Lagrangian, VOF and level set methods is shown in Figure 1.2

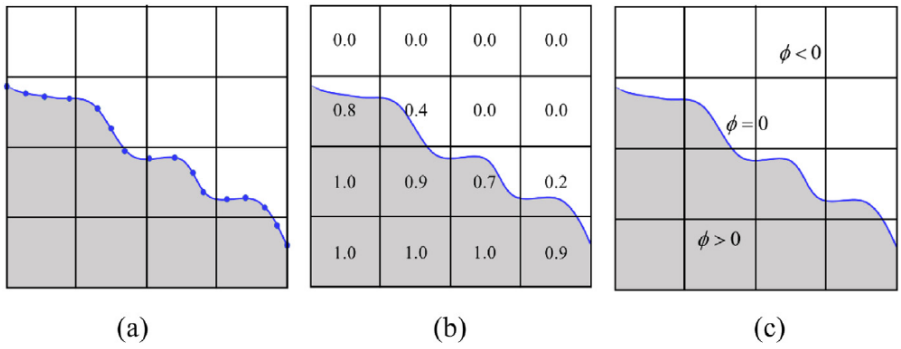

Figure 1.2 : Interface localization [1]: (a) Lagrangian. (b) VOF. (c) Level set.

Another important challenge is the estimation of the contact line velocity, which is also important for the calculation of the contact angle since the most of the DCA models express the contact angle as a function of the contact line velocity. In the Lagrangian techniques, the velocity of the marker particles can simply be used as the velocity of the contact line. In the Eulerian approach, many methods have been developed such as using the cell center velocity closest to the contact line [24], differentiation of the wetted radius [28], shear strain rate [29] or some complex set of equations.

Finally, one of the most important challenges is the estimation of the contact angle. Even though the earlier numerical studies on the problem didn't take the contact angle into account [30] or only considered a static contact angle [31], it is obvious that a DCA model is able to explain the phenomena more accurately since the problem itself is highly dynamic. Therefore, incorporating the DCA into the solution yields more robust results.

There are numerous proposed models to calculate the DCA [2, 32–36]. Besides, many parameters affect the outcome of these models. In this study, we have compared various DCA models with different flow settings against several experiments in order to evaluate their performances.

2. CONSERVATION EQUATIONS OF TWO-PHASE FLOW

The spreading of a droplet involves a liquid phase and a gaseous phase surrounding the liquid which is generally air. In our case, two immiscible, incompressible fluids are considered. We assume that phases are isothermal, so we are not concerned with the energy conservation.This section is devoted to present conservation equations of two phase flow, and it serves as a basis while deriving the VOF equations in the next section. We have used Sabisch's [37], Klitz's [3], Graveleau's [38] and Whittaker's [39] works as main resources while writing this and next section.

2.1 Flow Domain

Let us describe the open flow domain as $\Omega \subset \mathbb{R}^3$ and its boundary as Γ. Then, the closed flow domain is denoted as $\overline{\Omega} = \Omega \cup \Gamma$. We can now define two open subdomains, $\Omega_1 \subset \overline{\Omega}$ and $\Omega_2 \subset \overline{\Omega}$ for each phase such that

$$\overline{\Omega}_1 \cup \overline{\Omega}_2 = \overline{\Omega} \tag{2.1}$$

Since the two phases are assumed to be immiscible,

$$\Omega_1 \cap \Omega_2 = \varnothing \tag{2.2}$$

the interface between phases is defined as

$$\Gamma_f = \overline{\Omega}_1 \cap \overline{\Omega}_2. \tag{2.3}$$

and the boundaries of each phase are

$$\Gamma_k = (\overline{\Omega}_k \cap \Gamma) \cup \Gamma_f \tag{2.4}$$

where $k = \{1,2\}$ denotes different phases. Note that even though $\overline{\Omega}$ is not a function of time, Ω_1, Ω_2 and Γ_f are time dependent. An illustration of $\overline{\Omega}$ is given in Figure 2.1.

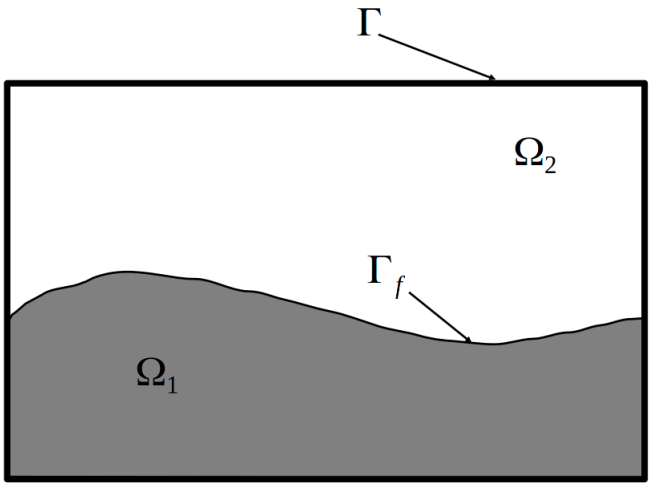

Figure 2.1 : An illustration of $\overline{\Omega}$.

2.2 Phase Tracking

A phase indicator function, $\mathbb{1}_k$, that specifies if a position vector, $\vec{x}$, is located at the domain of fluid k or not can be defined as

$$\mathbb{1}_k(\vec{x},t) = \begin{cases} 1 & \vec{x} \in \Omega_k(t) \\ 0 & otherwise. \end{cases} \tag{2.5}$$

We can then derive following relations:

$$\mathbb{1}_k^2 = \mathbb{1}_k \tag{2.6}$$

and

$$\mathbb{1}_k(1-\mathbb{1}_k) = 0 \tag{2.7}$$

Any flow variable, β, such as velocity or viscosity can be decomposed into two parts by making use of the indicator function such that:

$$\beta = \mathbb{1}_1\beta_1 + \mathbb{1}_2\beta_2. \tag{2.8}$$

2.3 Mass Conservation

By making use of equation (2.8), we can write velocity and density of the two phase flow as

$$u = \mathbb{1}_1 u_1 + \mathbb{1}_2 u_2 \tag{2.9}$$

and

$$\rho = \mathbb{1}_1\rho_1 + \mathbb{1}_2\rho_2 \tag{2.10}$$

Then, we can write the equation of mass conservation as

$$\frac{\partial(\mathbb{1}_1\rho_1 + \mathbb{1}_2\rho_2)}{\partial t} + \nabla(\mathbb{1}_1\rho_1\vec{u}_1 + \mathbb{1}_2\rho_2\vec{u}_2) = 0 \tag{2.11}$$

for the domain Ω. If a subdomain, for example Ω_1, is considered; substituting $\mathbb{1}_1 = 1$ and $\mathbb{1}_2 = 0$ into the above equation yields continuity for phase 1.

$$\frac{\partial\rho_1}{\partial t} + \nabla(\rho_1\vec{u}_1) = 0 \tag{2.12}$$

It is straightforward that for the phase 2, the continuity is

$$\frac{\partial\rho_2}{\partial 2} + \nabla(\rho_2\vec{u}_2) = 0 \tag{2.13}$$

Now that we have two equations for two phases, a boundary condition is needed to be defined at the phase interface.

At the interface, the mass conservation requires

$$\rho_1(\vec{u}_1 - \vec{u}_f)\cdot\vec{n}_f = \rho_2(\vec{u}_2 - \vec{u}_f)\cdot\vec{n}_f \quad at\ \Gamma_f \tag{2.14}$$

where u_f denotes the velocity of the phase interface and $\vec{n}_f$ denotes the normal to the interface. Besides that, if the interface is assumed to be impermeable, mass flux of a phase in the interface should be zero.

$$\rho_k(\vec{u}_k - \vec{u}_f)\cdot\vec{n}_f = 0 \quad at\ \Gamma_f \tag{2.15}$$

Combining this with the equation (2.14)

$$\vec{u}_k\cdot\vec{n}_f = \vec{u}_f\cdot\vec{n}_f \quad at\ \Gamma_f \tag{2.16}$$

and replacing u_f with u_k yields

$$\vec{u}_1\cdot\vec{n}_f = \vec{u}_2\cdot\vec{n}_f \quad at\ \Gamma_f \tag{2.17}$$

2.4 Momentum Conservation

Assuming the viscosity and density are constant for each phase, conservation of momentum equation can be written in a similar fashion to conservation of mass for each phase separately.

$$\rho_k \frac{\partial \vec{u}_k}{\partial t} + \rho_k (\vec{u}_k \nabla) \vec{u}_k = \nabla \boldsymbol{T}_k + \rho_k \vec{g} \tag{2.18}$$

Here, $\boldsymbol{T}_k$ is the stress tensor defined as $\boldsymbol{T}_k = P_k + \mu_k[\nabla \vec{u}_k + (\nabla \vec{u}_k)^T]$ where P_k is the pressure of phase k, μ_k is the dynamic viscosity of the phase k, $\vec{g}$ is the external volume forces and the superscript T denotes the transpose.

Boundary condition for the momentum equation is obtained by the stress balance at the interface:

$$\vec{n_f} \cdot (\boldsymbol{T}_1 - \boldsymbol{T}_2) = \sigma \vec{n_f} (\nabla \vec{n_f}) \tag{2.19}$$

The term in the right hand side accounts for surface tension, where σ is the surface tension coefficient between phases.

3. VOLUME OF FLUID EQUATIONS

In section 2, the conservation equations for two phase flow are derived. Those equations are defined in continuous space and time, therefore solving them computationally requires infinite memory and computation power. Hence, a discrete approximation of the conservation equation is required.

Firstly proposed by Hirt and Nichols [40], the VOF method has become an almost standard approach to deal with interfacial two phase flows numerically. In the VOF method, variables that represent cell averages are discretely defined in the cell centers. In this section, we will introduce the equations in the VOF method. The main idea behind the VOF method is averaging the conservation equations of individual phases and collect them to get one set of equations for multiphase flow. The variables of the new equations are defined in the cell centers of the computational cells. In order to obtain averaged equations, we first need to define two averaging operators, $\langle\cdot\rangle$ and $\langle\cdot\rangle_k$. The former one is called the superficial averaging operator and simply averages a variable defined in phase k over a volume

$$\langle\beta_k\rangle = \frac{1}{V}\int_V \beta_k dV \tag{3.1}$$

where V is the cell volume and V_k is the volume occupied by phase k. Whereas the latter one is called the intrinsic averaging operator and it averages the variable over the cell volume occupied by phase k, which is the space average to assign a single discrete value for a cell in finite volume analysis.

$$\langle\beta_k\rangle_k = \frac{1}{V_k}\int_{V_k} \beta_k dV \tag{3.2}$$

Alternative forms of the operators can be obtained by applying the statements (2.6), (2.7) and (2.8):

$$\langle\beta_k\rangle = \frac{1}{V}\int_{V_k} \beta_k \mathbb{1}_k dV = \frac{1}{V}\int_{V_k} \beta_k dV \tag{3.3}$$

$$\langle\beta_k\rangle_k = \frac{1}{V_k}\int_{V_k} \beta_k \mathbb{1}_k dV = \frac{1}{V_k}\int_{V_k} \beta_k dV \tag{3.4}$$

The relationship between the two averaging operators is:

$$\langle \beta_k \rangle = \frac{V_k}{V} \langle \beta_k \rangle_k \tag{3.5}$$

3.1 Volume Fraction

The volume fraction, also called color function, plays an important role in the VOF method. It is defined as the average of the indicator function over a computational cell:

$$\alpha_k = \langle \mathbb{1}_k \rangle = \frac{1}{V} \int_{V_k} \mathbb{1}_k dV \tag{3.6}$$

Since $\mathbb{1}_k$ is single valued and equal to 1 in phase k, the volume fraction is calculated as

$$\alpha_k = \frac{V_k}{V} \tag{3.7}$$

and it accounts for the volume occupied by phase k in the cell. Thus, $\alpha = 1$ means the cell is fully occupied by phase k and $\alpha = 0$ means the phase k does not exist in the cell. Any value between 0 and 1 indicates the presence of free surface in the cell (See Figure 3.1).

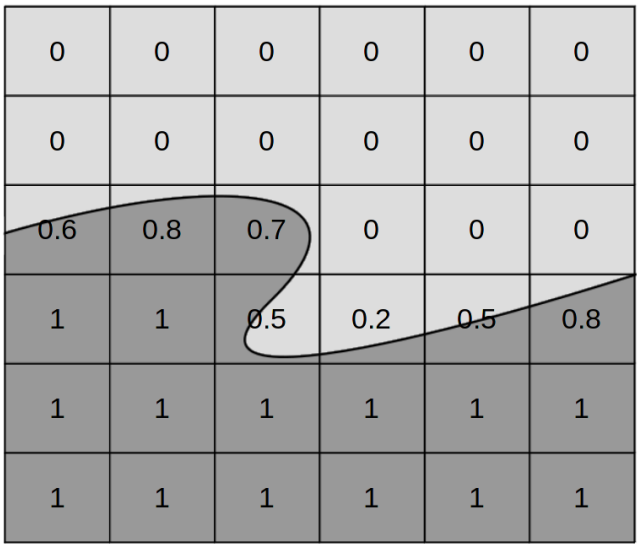

Figure 3.1 : Volume fraction field.

By introducing α we can now define variables of the two phase flow in terms of their phasic counterparts.

$$\langle \vec{u} \rangle = \alpha_1 \langle \vec{u}_1 \rangle_1 + \alpha_2 \langle \vec{u}_2 \rangle_2 \tag{3.8}$$

$$\langle p \rangle = \alpha_1 \langle p_1 \rangle_1 + \alpha_2 \langle p_2 \rangle_2 \tag{3.9}$$

$$\langle \rho \rangle = \alpha_1 \langle \rho_1 \rangle_1 + \alpha_2 \langle \rho_2 \rangle_2 \tag{3.10}$$

$$\langle \mu \rangle = \alpha_1 \langle \mu_1 \rangle_1 + \alpha_2 \langle \mu_2 \rangle_2 \tag{3.11}$$

If the assumptions of constant density and viscosity are made, then intrinsic averages of those terms posses no fluctuations, hence $\langle \rho_k \rangle_k = \rho_k$ and $\langle \mu_k \rangle_k = \mu_k$. By doing so, we can write the last two equations as follows

$$\langle \rho \rangle = \alpha_1 \rho_1 + \alpha_2 \rho_2 \tag{3.12}$$

$$\langle \mu \rangle = \alpha_1 \mu_1 + \alpha_2 \mu_2 \tag{3.13}$$

3.2 Conservation Equations in VOF Method

In the VOF method, conservation equations are generated by averaging their continuum counterparts and adding them up. Before taking that step, following averaging theorems need to be introduced.

$$\left\langle \frac{\partial \beta_k}{\partial t} \right\rangle = \frac{\partial \langle \beta_k \rangle}{\partial t} - \frac{1}{V} \int_{A_k} \beta_k \vec{u}_f \vec{n}_k dA \tag{3.14}$$

$$\langle \nabla \beta_k \rangle = \nabla \langle \beta_k \rangle + \frac{1}{V} \int_{A_k} \beta_k \vec{n}_k dA \tag{3.15}$$

Those theorems relate the derivative of the average to the average of the derivative where β_k is a scalar, $\vec{n}_k$ is the surface normal pointing from phase k to the other, $\vec{u}_f$ is the interface velocity.

3.3 Continuity

Continuity equation for phase 1 is given in equation (2.12). Averaging the continuity equation yields

$$\left\langle \frac{\partial \rho_1}{\partial t} + \nabla(\rho_1 \vec{u}_1) \right\rangle = \langle 0 \rangle \tag{3.16}$$

Since the averaging operator is linear, this can be written as:

$$\left\langle \frac{\partial \rho_1}{\partial t} \right\rangle + \nabla \langle \rho_1 \vec{u}_1 \rangle = \langle 0 \rangle \tag{3.17}$$

Applying averaging theorems (3.14) and (3.15) to the both terms in the left hand side of equation (3.17) yields:

$$\left\langle \frac{\partial \rho_1}{\partial t} \right\rangle = \frac{\partial \langle \rho_1 \rangle}{\partial t} - \frac{1}{V} \int_{A_1} \rho_1 \vec{u}_f \vec{n}_1 dA \tag{3.18}$$

$$\langle \nabla \rho_1 \vec{u}_1 \rangle = \nabla \langle \rho_1 \vec{u}_1 \rangle + \frac{1}{V} \int_{A_1} \rho_1 \vec{u}_1 \vec{n}_1 dA \tag{3.19}$$

Substituting the above equations into equation (3.17) results in:

$$\frac{\partial \langle \rho_1 \rangle}{\partial t} + \nabla \langle \rho_1 \vec{u}_1 \rangle = \frac{1}{V} \int_{A_1} \rho_1 \vec{n}_1 (\vec{u}_f - \vec{u}_1) dV \tag{3.20}$$

We can replace $\langle \rho_1 \rangle$ to its intrinsic counterpart using relations (3.5) and (3.7). Also making use of the incompressibility of individual phases, the mass conservation equation for phase 1 becomes:

$$\rho_1 \frac{\partial \alpha_1}{\partial t} + \rho_1 \nabla \alpha_1 \langle \vec{u}_1 \rangle = \frac{1}{V} \int_{A_1} \rho_1 \vec{n}_1 (\vec{u}_f - \vec{u}_1) dV \tag{3.21}$$

Similarly for the phase 2, we have:

$$\rho_2 \frac{\partial \alpha_2}{\partial t} + \rho_2 \nabla \alpha_2 \langle \vec{u}_2 \rangle = \frac{1}{V} \int_{A_2} \rho_2 \vec{n}_2 (\vec{u}_f - \vec{u}_2) dV \tag{3.22}$$

The terms in the right hand side describe the mass flow from one phase to the other. The boundary condition at the interface requires the mass flows to be equal, hence we can write the conservation of mass for both phases as

$$\frac{\partial \alpha}{\partial t} + \nabla \alpha \langle \vec{u}_1 \rangle = \frac{\dot{m}}{\rho_1} \tag{3.23}$$

and

$$\frac{\partial (1-\alpha)}{\partial t} + \nabla (1-\alpha) \langle \vec{u}_2 \rangle = -\frac{\dot{m}}{\rho_2} \tag{3.24}$$

where we have used $\alpha_1 = \alpha$ and $\alpha_2 = 1 - \alpha$. Mass conservation equation is obtained by adding up equations (3.23) and (3.24):

$$\nabla \langle \vec{u} \rangle = \dot{m} \Big(\frac{1}{\rho_1} - \frac{1}{\rho_2} \Big) \tag{3.25}$$

If there in no mass transfer between phases, the mass conservation equation is further reduced to

$$\nabla \langle \vec{u} \rangle = 0 \tag{3.26}$$

3.4 Momentum Conservation

We have described the Navier-Stokes equation for a single phase in equation (2.18). Averaging it yields:

$$\left\langle \frac{\partial}{\partial t}(\rho_k \vec{u}_k) \right\rangle + \langle \nabla(\rho_k \vec{u}_k \vec{u}_k) \rangle = \langle \nabla \boldsymbol{T}_k \rangle \tag{3.27}$$

With the averaging theorems, we can convert the average of the derivatives to the derivative of the averages:

$$\left\langle \frac{\partial}{\partial t}(\rho_k \vec{u}_k) \right\rangle = \frac{\partial}{\partial t}\langle \rho_k \vec{u}_k \rangle - \frac{1}{V}\int_{A_k} \rho_k \vec{u}_k \vec{u}_f \vec{n}_k dA \tag{3.28}$$

$$\langle \nabla(\rho_k \vec{u}_k \vec{u}_k) \rangle = \nabla \langle \rho_k \vec{u}_k \vec{u}_k \rangle + \frac{1}{V}\int_{A_k} \rho_k \vec{u}_k \vec{u}_k \vec{n}_k dA \tag{3.29}$$

$$\langle \nabla \boldsymbol{T}_k \rangle = \nabla \langle \boldsymbol{T}_k \rangle + \frac{1}{V}\int_{A_k} \boldsymbol{T}_k \vec{n}_k dA \tag{3.30}$$

Applying incompressibility assumption to those equations like we did in the continuity while deriving equation (3.21), we can simplify the first two equations above to:

$$\left\langle \frac{\partial}{\partial t}(\rho_k \vec{u}_k) \right\rangle = \rho_k \frac{\partial}{\partial t}(\alpha_k \langle \vec{u}_k \rangle) - \frac{1}{V}\int_{A_k} \rho_k \vec{u}_k \vec{u}_f \vec{n}_k dA \tag{3.31}$$

$$\langle \nabla(\rho_k \vec{u}_k \vec{u}_k) \rangle = \rho_k \nabla(\alpha_k \langle \vec{u}_k \vec{u}_k \rangle) + \frac{1}{V}\int_{A_k} \rho_k \vec{u}_k \vec{u}_k \vec{n}_k dA \tag{3.32}$$

Substituting them back into the equation (3.27) yields:

$$\rho_k \frac{\partial}{\partial t}(\alpha_k \langle \vec{u}_k \rangle) + \rho_k \nabla(\alpha_k \langle \vec{u}_k \vec{u}_k \rangle) = \nabla \langle \boldsymbol{T}_k \rangle + \frac{1}{V}\int_{A_k} \boldsymbol{T}_k \vec{n}_k dA \tag{3.33}$$

Here, the integrals in the inertial terms cancelled each other because of the boundary condition at the interface (equation (2.16)) which requires $\vec{u}_f = \vec{u}_k$. Momentum conservation equation for two phase flow is obtained by summing equation (3.33) for two phases

$$\rho \frac{\partial}{\partial t}\langle \vec{u} \rangle + \rho \nabla \langle \vec{u}\vec{u} \rangle = \nabla \langle T \rangle + F_\sigma \tag{3.34}$$

where F_σ is defined using the boundary condition at the interface. Since $n_1 = -n_2$, we can write

$$F_\sigma = \frac{1}{V}\int_A \sigma \vec{n}(\nabla \vec{n}) dA = \frac{1}{V}\int_A \vec{n}(\boldsymbol{T}_1 - \boldsymbol{T}_2) dA \tag{3.35}$$

In order to deal with the term $\langle \vec{u}\vec{u} \rangle$ in equation (3.34), we can split $\vec{u}$ into its average and a deviation part. Depending on the size of the cell, we may still have variation inside the cell. Therefore, when we assign a single discrete value to the cell center representing the spatial average of the variable under consideration, we must have a deviation component, $\vec{u}'$, representing variation of the variable within the cell. Hence, similar to Reynolds decomposition, we can write,

$$\vec{u} = \langle \vec{u} \rangle + \vec{u}' \tag{3.36}$$

We expect that theoretically as the cell volume shrinks to zero, the variational part should go to zero as well. With this decomposition, we can write,

$$\langle \vec{u}\vec{u} \rangle = \langle (\langle \vec{u} \rangle + \vec{u}')(\langle \vec{u} \rangle + \vec{u}') \rangle \tag{3.37}$$

$$\langle \vec{u}\vec{u} \rangle = \langle \langle \vec{u} \rangle \langle \vec{u} \rangle \rangle + \langle \langle \vec{u} \rangle \vec{u}' \rangle + \langle \vec{u}' \langle \vec{u} \rangle \rangle + \langle \vec{u}'\vec{u}' \rangle \tag{3.38}$$

since the spatial average of the variational part is zero.

$$\langle \vec{u}\vec{u} \rangle = \langle \langle \vec{u} \rangle \langle \vec{u} \rangle \rangle + \langle \vec{u}'\vec{u}' \rangle \tag{3.39}$$

$\langle \vec{u}'\vec{u}' \rangle$ approaches to zero as the averaging volume gets smaller. So while using fine meshes this term becomes less significant and we can approximate $\langle \vec{u}\vec{u} \rangle$ as $\langle \vec{u} \rangle \langle \vec{u} \rangle$.

In addition to above approximation, we approximate the viscous term in the stress tensor as $\nabla\mu(\langle \nabla\vec{u} \rangle + \langle \nabla\vec{u} \rangle^T)$ and finalize the VOF formulation of momentum conservation.

$$\rho \frac{\partial}{\partial t} \langle \vec{u} \rangle + \rho \nabla \langle \vec{u} \rangle \langle \vec{u} \rangle = \nabla \langle P \rangle + \nabla\mu(\langle \nabla\vec{u} \rangle + \langle \nabla\vec{u} \rangle^T) + F_\sigma \tag{3.40}$$

3.5 Phase Fraction Equation

While combining two sets of conservation equations into one we have introduced a new variable, phase fraction. The equation for phase fraction can be obtained by manipulating the averaged mass conservation equation for single phase. Introducing relative velocity as

$$\langle \vec{u}_r \rangle = \langle \vec{u}_1 \rangle - \langle \vec{u}_2 \rangle \tag{3.41}$$

averaged velocity of the phase 1 can be written as

$$\langle \vec{u}_1 \rangle = \langle \vec{u} \rangle + (1-\alpha)\langle \vec{u}_r \rangle \tag{3.42}$$

inserting the equation (3.42) into equation (3.23), we obtain the equation for the phase fraction

$$\frac{\partial \alpha}{\partial t} + \nabla(\alpha \langle \vec{u} \rangle) + \nabla(\alpha(1-\alpha)\langle \vec{u}_r \rangle) = \frac{\dot{m}}{\rho_1} \tag{3.43}$$

$(\alpha(1-\alpha)\langle \vec{u}_r \rangle)$ is generally referred to as compression term, it compresses the free surface and provides a sharper interface. It acts only on the interface region because the term $\alpha(1-\alpha)$ is equal to zero if α is either zero or one.

4. CONTACT ANGLE

The contact angle is the angle between the interface of the two fluids and the solid surface. When contact line is stationary, the contact angle is a property of the fluids-solid system and called as equilibrium contact angle, θ_E. The relationship between surface tensions of the phases and equilibrium contact angle on an ideal surface is shown by Thomas Young [41] as

$$Cos(\theta_E)\vec{\sigma}_{LG} = \vec{\sigma}_{SG} - \vec{\sigma}_{SL} \tag{4.1}$$

Here, σ_{LG}, σ_{SG} and σ_{SL} are surface tensions of liquid-gas, solid-gas and solid-liquid, respectively. An illustration of the surface tensions and contact angle can be seen in Figure 4.1.

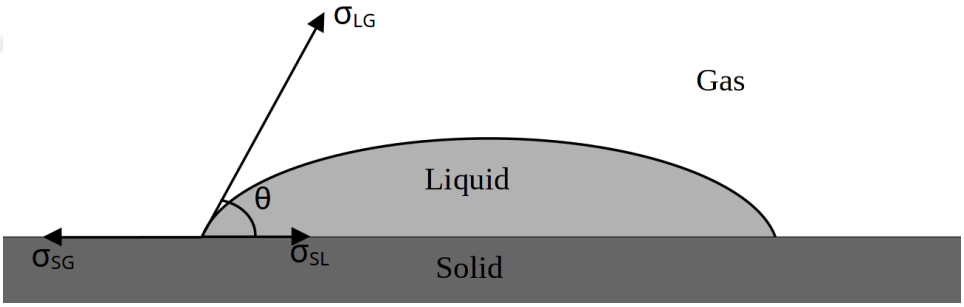

Figure 4.1 : Contact angle and surface tension.

In fact, the equation (4.1) is an exception rather than a rule, and the equilibrium contact angle takes a value between the advancing contact angle (θ_A) and the receding contact angle (θ_R).

$$\theta_R \leq \theta_E \leq \theta_A \tag{4.2}$$

Advancing contact angle is the contact angle measured just before the contact line begins its movement to expand the liquid phase, similarly receding contact angle is the contact angle measured just before the contact line begins its movement to expand the gas phase (See Figure 4.2(b)). The difference between the advancing and the receding

contact angles is called contact angle hysteresis:

$$H = \theta_A - \theta_D \tag{4.3}$$

It is generally viewed as a result of chemical heterogeneity of the surface and surface roughness [35, 42], but still is a controversial subject [43, 44].

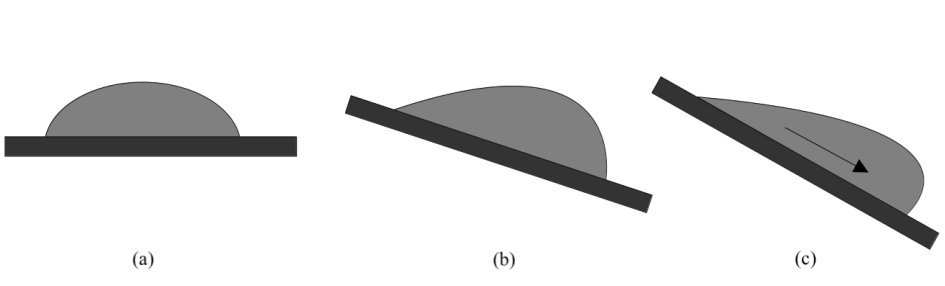

Figure 4.2 : Contact angles: (a) Equilibrium contact angle. (b) Contact angle hysteresis. (c) Dynamic contact angle.

When the contact line moves, the contact angle deviates from its equilibrium value and is called the dynamic contact angle (θ_D). In the dynamic situation, Young's equation is no longer able to explain contact angle since there is no equilibrium. If the contact line is advancing, in other words, it moves from liquid to gas, the DCA is greater than the equilibrium one. Similarly for a receding contact line, the DCA is less than the equilibrium contact angle (See Figure 4.2(c)). Although a general and accurate way of calculating the DCA in relation to flow and fluid properties has not yet been found, many attempts have been made to model the contact angle.

One of the pioneering works on DCAs is from Hoffman [45]. From his experiments he observed that the DCA is a function of Capillary number and a shift factor,

$$\theta_D = f(Ca + F(\theta_E)) \tag{4.4}$$

where the shift factor, F, is an unknown function of equilibrium contact angle and Capillary number is the ratio of viscous forces to the surface tension:

$$Ca = \frac{\mu u_{cl}}{\sigma} \tag{4.5}$$

where u_{cl} is contact line velocity. However Hoffman did not propose a complete formulation.

In 1993, Kistler presented an empirical model based on Hoffman's observations [32]. Kistler's correlation for the DCA is,

$$\theta_D = f_{hoff}(Ca + f_{hoff}^{-1}(\theta_E)) \tag{4.6}$$

where f_{hoff}^{-1} is the inverse of the Hoffman function and Hoffman function is defined as:

$$f_{hoff}(x) = Cos^{-1}\Big\{1 - 2Tanh\Big[5.16\Big(\frac{x}{1+1.31x^{0.99}}\Big)^{0.706}\Big]\Big\} \tag{4.7}$$

The DCA model based on Shikhmurzaev's theoretical studies on the moving contact lines [34] is of the form

$$Cos(\theta_D) = Cos(\theta_E) - \frac{2u^*(a_1 + a_2 u_0^*)}{(1-a_2)\big((a_1+u^{*2})^{1/2} + u^*\big)} \tag{4.8}$$

$$u^* = a_3 \frac{\mu_l u_{cl}}{\sigma}$$

$$u_0^* = \frac{Sin(\theta_D) - \theta_D Sin(\theta_D)}{Sin(\theta_D)Cos(\theta_D) - \theta_D}$$

$$a_1 = 1 + (1-a_2)(Cos(\theta_E) - a_4)$$

where a_2, a_3 and a_4 are phenomenological constants. For water these constants are given as $a_2 = 0.54$, $a_3 = 12.5$, $a_4 = -0.07$ and for glycerin $a_2 = 0.63$, $a_3 = 4.3$, $a_4 = -0.08$ [46, 47].

Another DCA model we use in this work is the Bracke's empirical correlation [36]:

$$Cos(\theta_D) = Cos(\theta_E) - 2(1 + Cos(\theta_E))Ca^{1/2} \tag{4.9}$$

Quasi-Dynamic contact angle model is the simplest DCA model. In this model the value of the DCA depends only on the sign of the contact line velocity, i.e. whether if the contact line is advancing or receding.

$$\theta_D = \begin{cases} \theta_A & if \;\; u_{cl} > 0 \\ \theta_E & if \;\; u_{cl} = 0 \\ \theta_R & if \;\; u_{cl} < 0 \end{cases} \tag{4.10}$$

In the absence of the hysteresis data, this model reduces to static contact angle model.

$$\theta_D = \theta_E \tag{4.11}$$

All of the models above except the Quasi-Dynamic model predict DCAs for advancing contact lines only. However, many researchers successfully used the Kistler model for

both receding and advancing contact lines in numerical simulations [18, 21, 28, 48], which is also the approach we adopted in this work. On the other hand, we use a different approach for the Shikhmurzaev and the Bracke models [46, 49]. The Hoffman-Voinov-Tanner law,

$$\theta_D^3 = \theta_R^3 - 72Ca \tag{4.12}$$

is used to estimate the dynamic receding contact angle for those models. The estimated contact angles by each DCA model we have used at different contact line velocities for water on a smooth wax surface ($\theta_A = 105^\circ$ and $\theta_R = 95^\circ$) are shown in Figure 4.3.

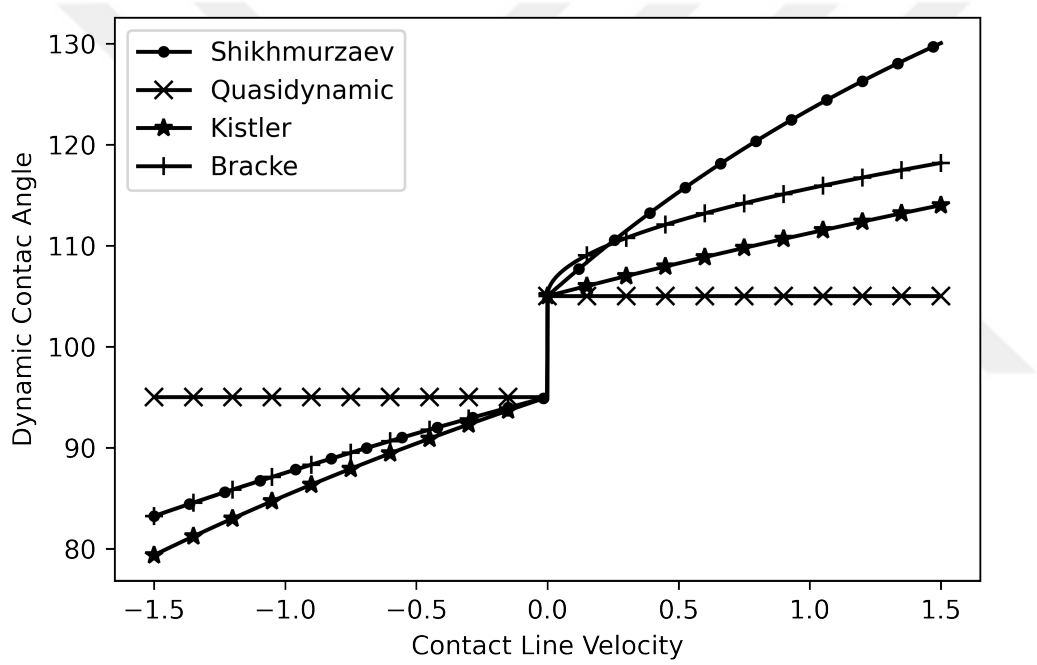

Figure 4.3 : DCA versus contact line velocity for different DCA models.

The contact angle hysteresis is incorporated into the models by replacing θ_E with θ_A and θ_R in case of advancing and receding contact lines, respectively.

5. METHODOLOGY

5.1 Experiments

In order to compare the effect of the contact angle models on the simulation accuracy, 5 experiments are chosen. In all of the experiments, a liquid droplet is impinged on a solid, smooth, dry and flat surface. The experiments are chosen in order to ensure a variety of Reynolds and Weber numbers are covered. The simulated experiments' specifications are given in Table 5.1 and properties of water and glycerin are given in Table 5.2.

Table 5.1 : Experiments.

Case	Liquid	Wall	We	Re	U_0	D_0	θ_A	θ_R	Ref
1	Water	Wax	52	3245	1.18	2.75	105	95	[50]
2	Water	Wax	90	4010	1.64	2.45	105	95	[51]
3	Glycerin	Wax	93	36	1.41	2.45	97	90	[51]
4	Water	S. Steel	7.9	1200	0.48	2.5	120	65	[52]
5	Water	S. Steel	1.81	575	0.23	2.5	120	65	[52]

Table 5.2 : Properties of liquids.

Liquid	σ [N/m]	$\mu[mPas]$	$\rho[kg/m^3]$
Water	0.073	1	996
Glycerin	0.063	116	1220

In this context, Reynolds and Weber numbers are defined as:

$$Re = \frac{\rho_l u_0 D_0}{\mu_l} \tag{5.1}$$

$$We = \frac{\rho_l u_0^2 D_0}{\sigma_{LG}} \tag{5.2}$$

5.2 Numerical implementation

For the numerical computations, we've used OpenFOAM's two phase flow solvers, interFoam [53] and interFlow [54]. They are both VOF method implementations for immiscible, incompressible and isothermal fluids. We have explained the VOF equations in detail in section 3. In summary, they are:

$$\nabla \vec{u} = 0 \tag{5.3}$$

$$\frac{\partial}{\partial t}(\rho \vec{u}) + \nabla(\rho \vec{u}\vec{u}) = -\nabla p + \nabla \mu(\nabla \vec{u} + \nabla \vec{u}^T) + F_\sigma + \rho \vec{g} \tag{5.4}$$

$$\frac{\partial \alpha}{\partial t} + \nabla(\alpha u) + \nabla \alpha(1-\alpha)\vec{u}_r = 0 \tag{5.5}$$

where we have dropped the brackets that denote average values.

In order to keep the interface sharp, interFoam uses Multidimensional Universal Limiter with Explicit Solution limiter (MULES) which models the relative velocity on the cell face in equation (5.5) as

$$\vec{u}_{r,f} = \vec{n}_f \; min\left(C_\alpha \frac{|\phi|}{|S_f|}, max\left(\frac{|\phi|}{|S_f|} \right) \right) \tag{5.6}$$

where ϕ is the face flux, S_f is the face area vector normal to the face pointing out of the cell, $\vec{n}_f$ is the interface normal and C_α is a user defined compression coefficient [55]. One problem of the MULES algorithm is, the interface is smeared over a small number of cells [56].

The IsoAdvector method is a geometrical scheme for advection of sharp interfaces, proposed as a replacement for MULES [54]. It is reported that it can successfully solve the smearing problem of the MULES algorithm. The IsoAdvector method cuts the cells into two parts so that each part contains only one fluid. In order to cut a cell, the IsoAdvector method interpolates the cell centered phase fractions to cell vertices, then using these vertices it decides where to cut the cell [57]. We have conducted numerical computations using both MULES and IsoAdvector.

For the pressure-velocity coupling Pressure Implicit with Splitting of Operator (PISO) algorithm is used. Discretization schemes that we have used are given in Appendix

A. An adjustable time step scheme is used and time steps are adjusted so that Courant–Friedrichs–Lewy (CFL) number never exceeds 0.2.

5.2.1 Surface tension

The surface tension force, F_σ is given in equation (3.35) as

$$F_\sigma = \frac{1}{V}\int_A \sigma\vec{n}(\nabla\vec{n})dA \tag{5.7}$$

however, it is not possible to compute that as it is. The method used to calculate F_σ is Brackbill's continuum surface force model [58]. This model computes the surface force as

$$F_\sigma = \sigma\kappa\nabla\alpha \tag{5.8}$$

where κ denotes the curvature of the phase interface and it is defined as

$$\kappa = \nabla\vec{n} \tag{5.9}$$

and the unit normal, $\vec{n}$ is

$$\vec{n} = \frac{\nabla\alpha}{|\nabla\alpha|} \tag{5.10}$$

5.2.2 Computational domain

The computational domain of the simulations is an axisymmetric wedge of 5° with 10 mm radius and 10 mm height as shown schematically in Figure 5.1. By setting the domain radius to 10 mm, we ensured that the radius of the domain is 7-8 times higher than the initial droplet radius.

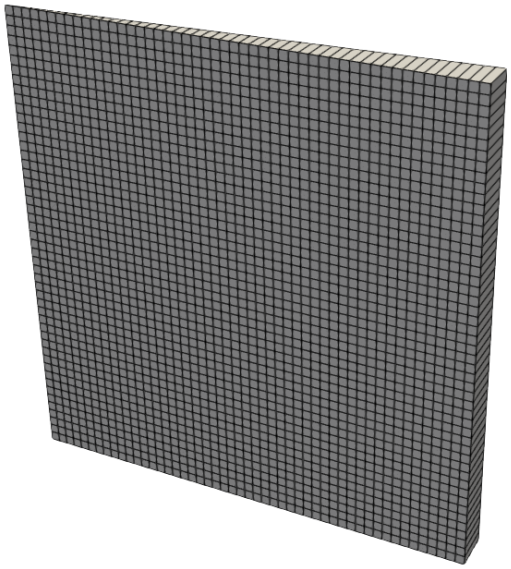

Figure 5.1 : Schematic view of computational domain.

The mesh has one cell in azimuthal direction and uniformly spaced cells in non-azimuthal directions. In order to ensure grid independency, mesh convergence study is conducted and results are given in Section 6.1. According to the mesh convergence study, 500×500 grid is selected which is composed of 20 μm × 20 μm cells.

5.2.3 Initial and boundary conditions

Since we are conducting axisymmetric computations, wedge boundary condition is used at the front and back planes of the domain. Contact angle models described in Section 4 are implemented and used as boundary condition at the wall for the phase fraction coupled with no-slip boundary condition for the velocity. At all other boundaries, the phase fraction is set to zero and velocities are defined as inlet-outlet. The pressure boundary conditions are set to zero gradient at the wall and prescribed atmospheric pressure at the other boundaries.

The initial geometry of the droplet is formed by setting phase fraction field at corresponding cells before the simulation starts and impact velocity of the droplet is set in the same manner. The initial state of the domain and boundary conditions can be seen in Figure 5.2.

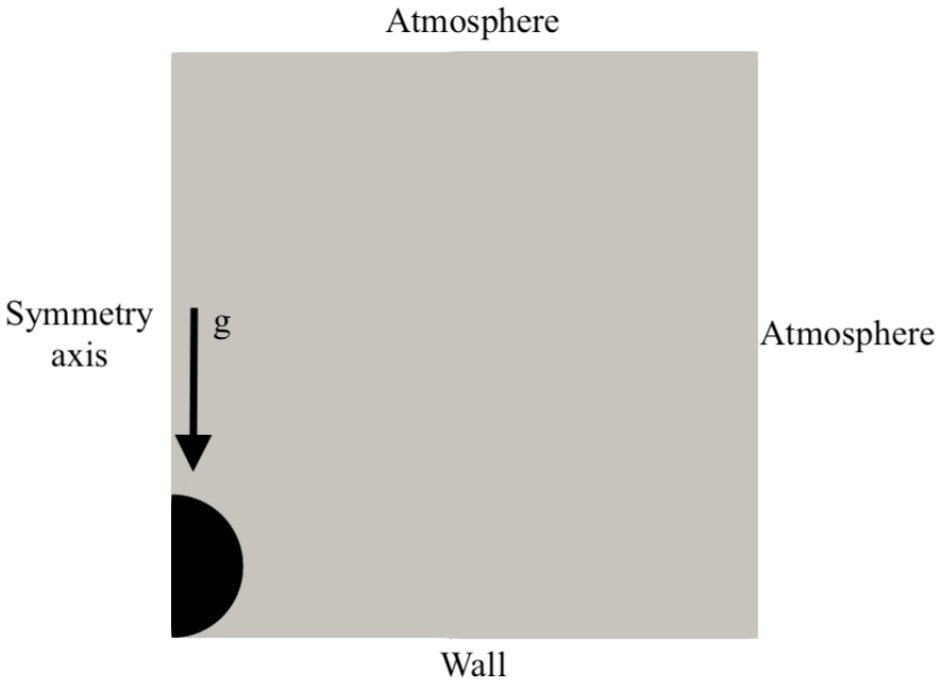

Figure 5.2 : Initial state of the computational domain.

5.2.4 Contact line velocity

As stated in Section 4, all of the DCA models we use depend on contact line velocity, u_{cl}, through Ca or sign of the u_{cl}. We calculate the contact line as parallel component of the cell center velocity closest to the wall as;

$$u_{cl} = |\vec{u}_{cl}| = \vec{n}_{parallel} \cdot \vec{u}_{parallel} \tag{5.11}$$

where $\vec{u}_{parallel}$ and $\vec{n}_{parallel}$ are velocity and interface normal's components parallel to the wall. Or explicitly ;

$$u_{cl} = \frac{\vec{n} - (\vec{t} \cdot \vec{n})\vec{t}}{|\vec{n} - (\vec{t} \cdot \vec{n})\vec{t}|} \cdot \left(\vec{u} - (\vec{t} \cdot \vec{u})\vec{t}\right) \tag{5.12}$$

where $\vec{n}$ is the phase interface normal, $\vec{t}$ is the wall normal and $\vec{u}$ is the fluid velocity.

6. RESULTS AND DISCUSSION

6.1 Mesh Convergence

In numerical simulations of fluid dynamics problems, it is important to have results not affected by the selected grid size. Therefore, a mesh convergence test is conducted in order to ensure that the solution is independent from mesh size. Usually finer meshes yield more accurate solutions, but they come with the cost of computation time. So it is important to find a mesh size that gives accurate results and has low computation time.

In this study, mesh sizes of 200×200, 250×250, 500×500, 625×625, 800×800 and 1000×1000 are tested. In Figure 6.1, temporal evolution of spread factor is plotted for Case 2 using the Kistler contact angle model. The spread factor (D/D_0) is defined as the ratio of the wetted radius and the initial radius of the droplet.

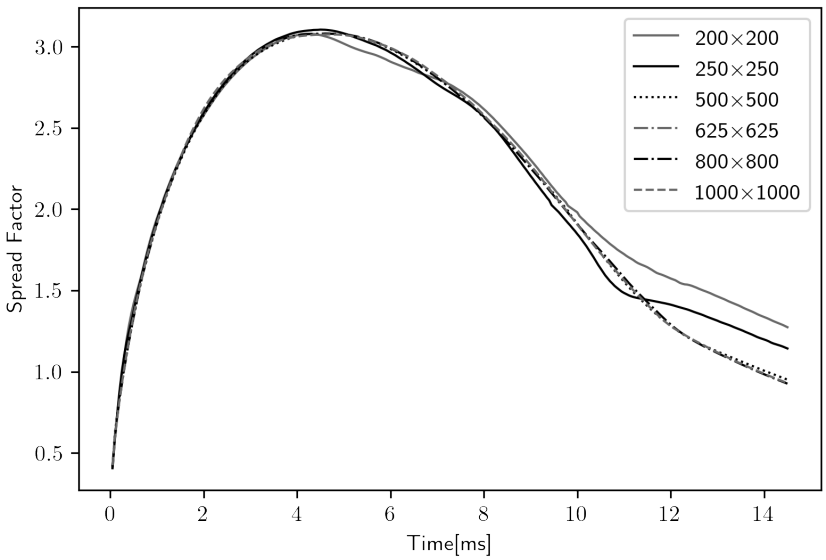

Figure 6.1 : Mesh convergence study results.

It seems that the results become independent of the mesh size only after 500×500 resolution. It can be seen that 500×500 mesh is almost accurate as finer mesh

resolutions and it requires much less computational effort as shown in Table 6.1. We have selected 500×500 mesh size which corresponds to 20 μm × 20 μm cells.

Table 6.1 : Computation times of different mesh sizes.

Mesh Size	Computation Time
200×200	565s
250×250	844s
500×500	10325s
625×625	24404s
800×800	37406s
1000×1000	70639s

6.2 Numerical Simulations of Droplet Spread Experiments

In this section, we will present the results of the numerical simulations of droplet spread experiments introduced in section 5.1. In the numerical simulations, we have compared four DCA models, namely the Quasi-Dynamic, the Kistler, the Shikhmurzaev and the Bracke models. We have also compared two interface capturing schemes; an algebraic scheme MULES and a geometrical scheme IsoAdvector.

We will evaluate the performance of the contact angle models qualitatively by comparing the images taken from the simulations at particular time instants. These instants are chosen to enable us to make a comparison between the real images of the droplets given in the experiments [28, 50, 52].

Quantitative analyses are done by comparing the maximum spread diameter and temporal evolution of the spread factor. The mean spread factor error (MSFE) is measured by averaging the relative absolute difference between different instants in the experiment and the simulation. The maximum spread diameter error (MSDE) is measured by normalizing the maximum spread diameter difference between the simulations and the experiment. The normalization is done by dividing the difference to the value of the corresponding experimental data.

Although it is a common practice in droplet spread studies to use non dimensional time, for comparison with the experimental images, we have not nondimensionalized our results. The dimensionless time is defined as

$$\tau = \frac{tU_0}{D_0} \tag{6.1}$$

where t is time, U_0 is impact velocity and D_0 is initial droplet diameter.

6.2.1 Case 1

In this case a water droplet of 2.75 mm diameter impacts onto a wax surface with 1.18 m/s initial velocity. Reynolds and Weber numbers are 3245 and 52 respectively. The surface is slightly hydrophobic with contact angles $\theta_A = 105^\circ$ and $\theta_R = 95^\circ$.

In the first 3 ms, where the spreading occurs, all the contact angle models used in conjunction with either the MULES or the IsoAdvector schemes predict spreading diameter reasonably well. After 1.5 ms, the difference between contact angle models become distinguishable as shown in Figure 6.2. At the maximum spread stage, roughly

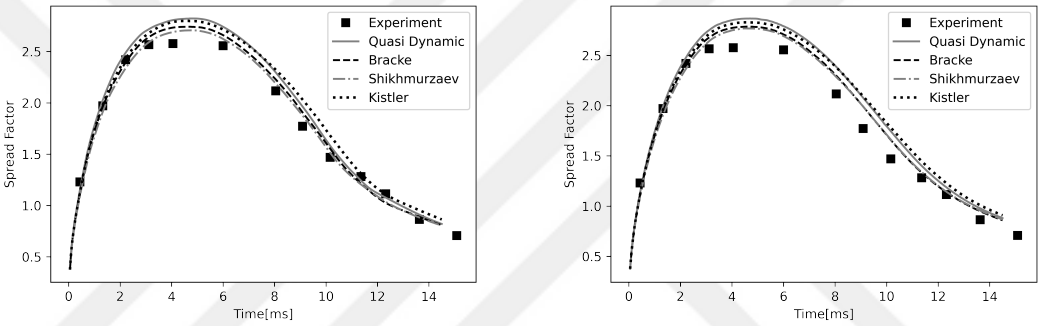

MULES IsoAdvector

Figure 6.2 : Comparison of DCA models in terms of spread factor for Case 1.

between 3 ms and 6 ms, all DCA models overestimate the radius of the droplet. The order of overestimation is same in both the MULES and the IsoAdvector simulations and, in descending order, appears as the Quasi-Dynamic, the Kistler, the Bracke and the Shikhmursaev models in descending order. After the maximum spread, roughly after 6 ms, the droplet starts to recoil. As can be seen in Figure 6.3, in the MULES simulations all of the DCA models seem to capture the recoiling stage well, whereas in the IsoAdvector simulations spread diameter is slightly higher compared to the experiment.

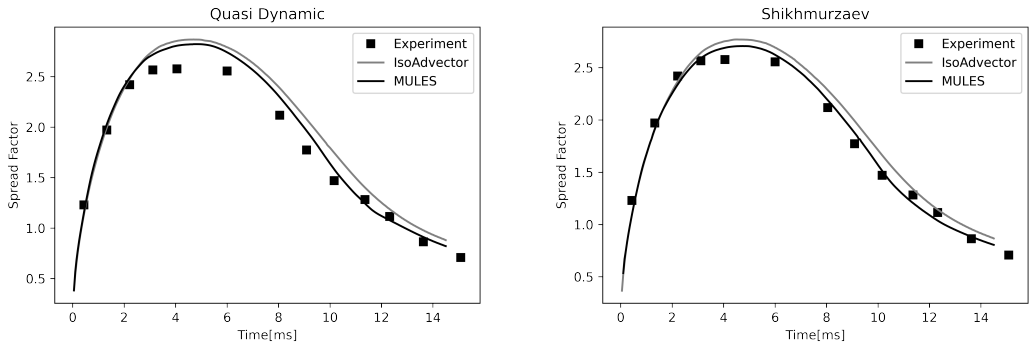

Quasi-Dynamic Shikhmurzaev

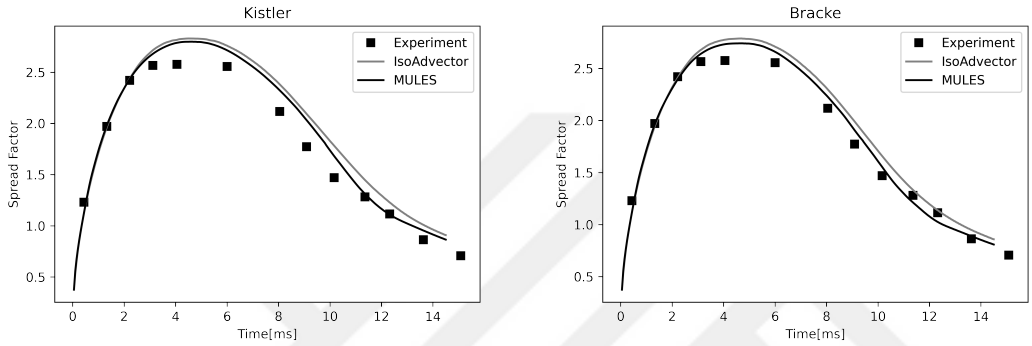

Kistler Bracke

Figure 6.3 : Comparison of MULES and IsoAdvector in terms of spread factor for Case 1.

All contact angle models perform better when they are coupled in the MULES algorithm compared to the IsoAdvector. The Shikhmurzaev model has the best accuracy in terms of both MSFE and MSDE, followed by the Bracke model. Errors of all models are listed in Table 6.2.

Table 6.2 : MSFE and MSDE of the simulations for Case 1.

Interface Method	DCA Model	MSFE	MSDE
MULES	Shikhmurzaev	4.18%	5.03%
MULES	Kistler	7.75%	8.60%
MULES	Bracke	4.89%	6.39%
MULES	Quasi-Dynamic	7.05%	9.52%
IsoAdvector	Shikhmurzaev	7.15%	7.47%
IsoAdvector	Kistler	11.33%	9.82%
IsoAdvector	Bracke	7.17%	8.20%
IsoAdvector	Quasi-Dynamic	10.76%	11.31%

In the earlier stages of impingement, the shapes of the droplets are almost identical except for the air bubble formation observed in IsoAdvector simulations (See Figure

6.4 and Figure 6.5). The gray areas in the MULES simulations, which can be seen starting from the earliest time instances, grow as time goes on, and are the result of the diffusive nature of the algorithm. Unlike MULES, the IsoAdvector method is able to generate a sharp interface and, therefore, the gray areas don't appear in the IsoAdvector simulations.

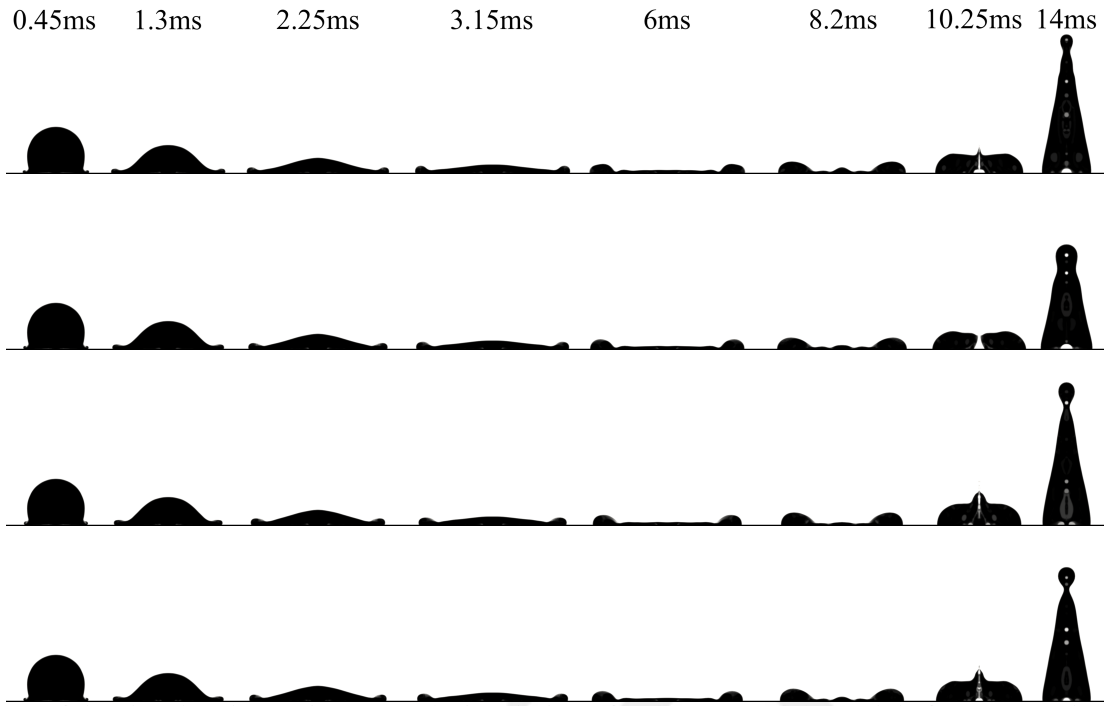

Figure 6.4 : Temporal evolution of the droplet shapes is MULES simulations for Case 1. DCA models from top to bottom: Quasi-Dynamic, Kistler, Shikhmurzaev and Bracke.

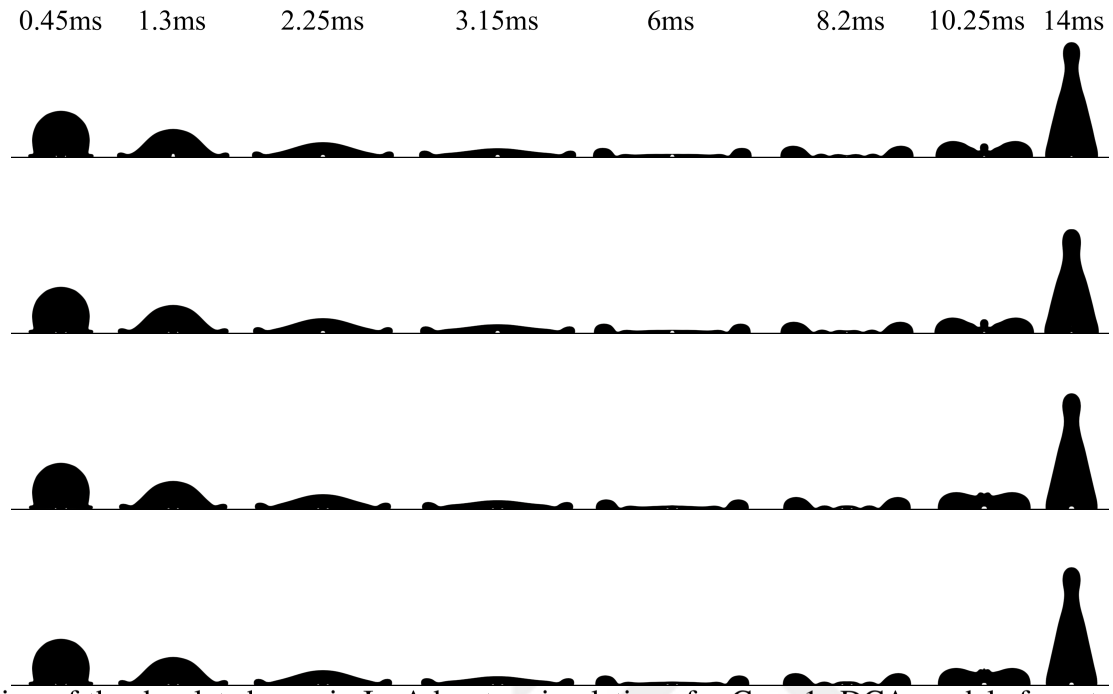

Figure 6.5 : Temporal evolution of the droplet shapes in IsoAdvector simulations for Case 1. DCA models from top to bottom: Quasi-Dynamic, Kistler, Shikhmurzaev and Bracke.

6.2.2 Case 2

In the second case, we will investigate a configuration similar to the first case where a water droplet impacts onto a wax surface with Weber Number of 90 and Reynolds Number of 4010. The diameter of the water droplet in this case 2.45 mm and the impact velocity is 1.64 m/s.

In the spreading stage, the numerical simulations predict the spread factor to be greater than the experiment, but in the recoiling stage they tend to predict lower spread factors as shown in Figure 6.6. Unlike the case 1, all of the DCA models perform better in the IsoAdvector simulations (See Figure 6.7). We can see that in the MULES simulations, except for the Shikhmurzaev model, all the DCA models start to recede earlier than the experiment.

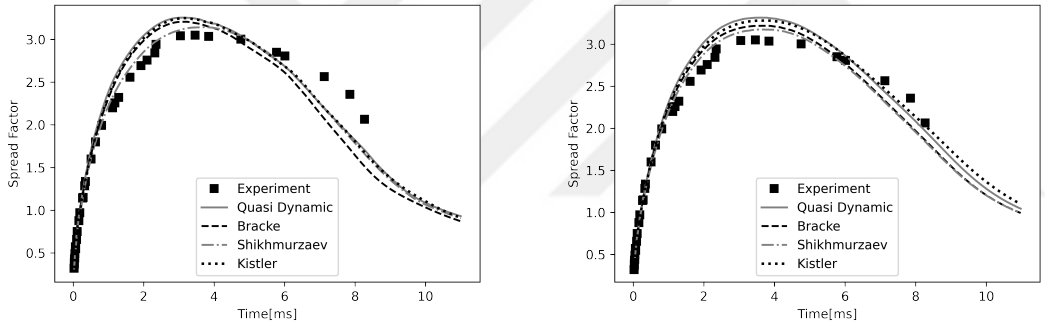

MULES IsoAdvector

Figure 6.6 : Comparison of DCA models in terms of spread factor for Case 2.

The temporal evolution of the numerical results agrees well with the experiment. However, the microdroplets that vertically emerge from the main droplet body can be seen in all four DCA models in the MULES, and only for the Shikhmurzaev model in the IsoAdvector at 11 ms, as shown in Figure 6.8 and Figure 6.9, but this feature is not observed in the experiment.

Overall, all of 8 simulations result in low errors as can be seen in Table 6.3, but the Shikhmurzaev model gives the best results for both spread factor and maximum spread diameter just like in Case 1.

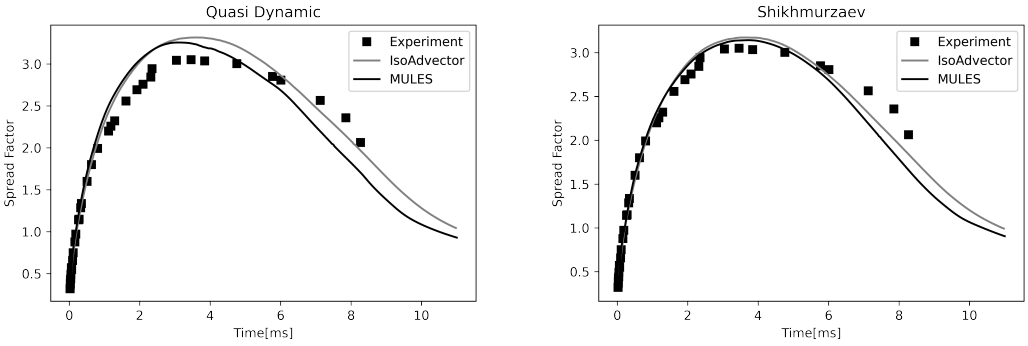

Quasi-Dynamic Shikhmurzaev

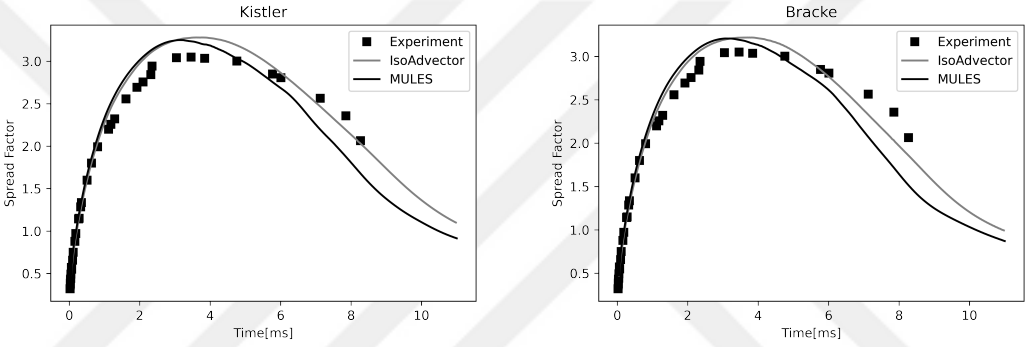

Kistler Bracke

Figure 6.7 : Comparison of MULES and IsoAdvector in terms of spread factor for Case 2.

Table 6.3 : MSFE and MSDE of the simulations for Case 2.

Interface method	DCA Model	MSFE	MSDE
MULES	Shikhmurzaev	5.91%	3.06%
MULES	Kistler	7.79%	6.55%
MULES	Bracke	8.93%	5.15%
MULES	Quasi-Dynamic	8.49%	6.72%
IsoAdvector	Shikhmurzaev	5.01%	4.06%
IsoAdvector	Kistler	5.51%	7.55%
IsoAdvector	Bracke	5.66%	5.53%
IsoAdvector	Quasi-Dynamic	6.56%	8.69%

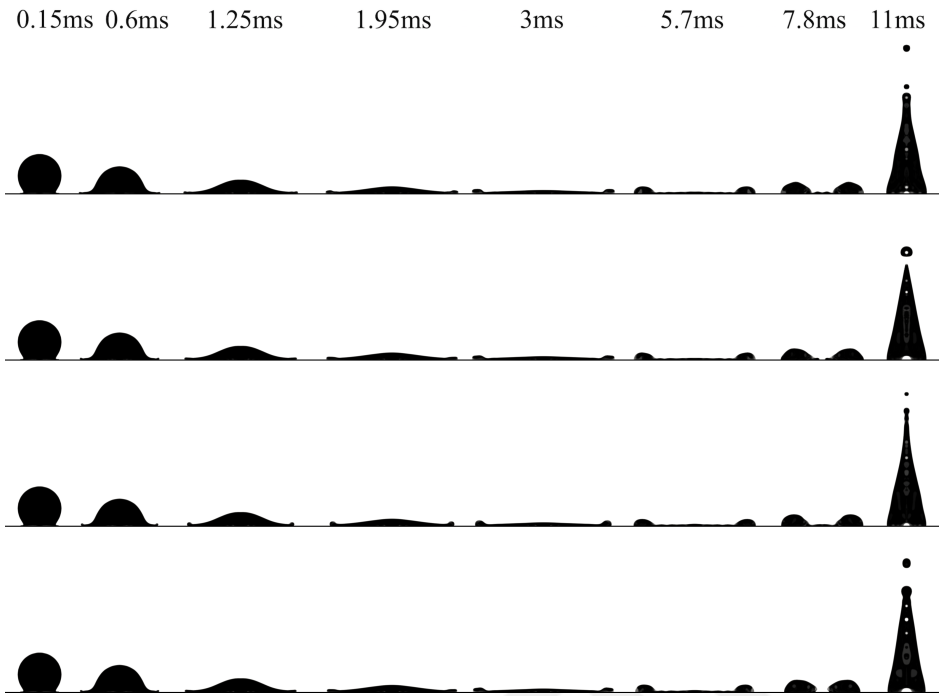

Figure 6.8 : Temporal evolution of the droplet shapes in MULES simulations for Case 2. DCA models from top to bottom: Quasi-Dynamic, Kistler, Shikhmurzaev and Bracke.

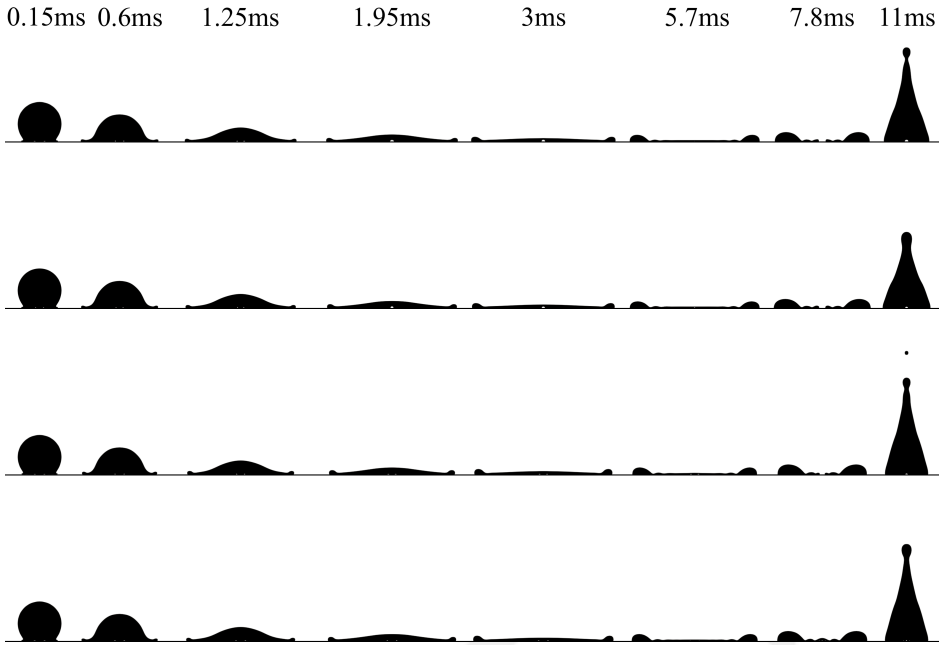

Figure 6.9 : Temporal evolution of the droplet shapes in IsoAdvector simulations for Case 2. DCA models from top to bottom: Quasi-Dynamic, Kistler, Shikhmurzaev and Bracke.

6.2.3 Case 3

This case is a low Reynolds number case where a glycerin droplet of 2.45 mm diameter impacts onto a wax surface with 1.41 m/s initial velocity. Reynolds and Weber numbers are 36 and 93, respectively. The surface is slightly hydrophobic with contact angles $\theta_A = 97^\circ$ and $\theta_R = 90^\circ$.

In all simulations, the air entrapment between the wall and the droplet is observed and this happens probably due to the high viscosity of glycerin as can be seen in Figure 6.12 and Figure 6.13. The spreading stage is captured very well with all contact angle models in both the MULES and the IsoAdvector simulations. The Bracke and the Shikhmurzaev models started to recede after the spreading stage and this is not observed in the experiment (See Figure 6.10). We can see a smaller rebound in Quasi-Dynamic model as well, but it is much slower compared to the Shikhmurzaev and the Bracke models. The Kistler model on the other hand is able to keep the spread factor at its maximum value over the time.

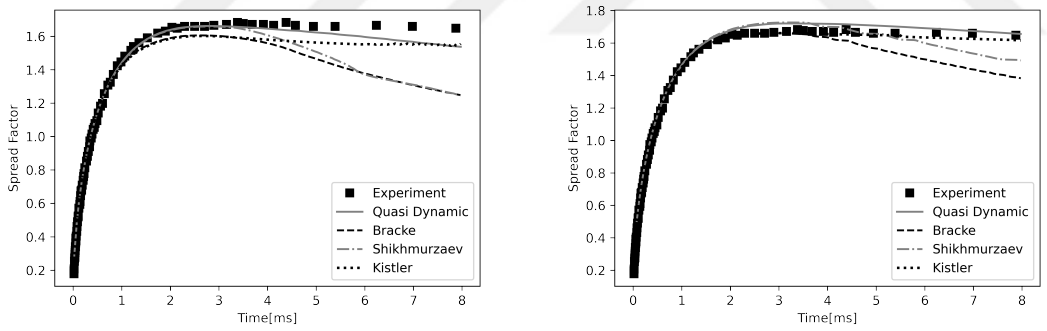

MULES IsoAdvector

Figure 6.10 : Comparison of DCA models in terms of spread factor for Case 3.

The Kistler model coupled with the IsoAdvector has almost a perfect match to the experimental results, but a slight underestimation of the spread factor is present in the MULES simulation (See Figure 6.11). In overall, we can say that the MULES simulations always underestimate the spread factor compared to the IsoAdvector. The MSFE and MSDE values for the Case 3 in given in Table 6.4. Unlike the high Reynolds number cases, in this case, the MULES is also able to keep the interface sharp.

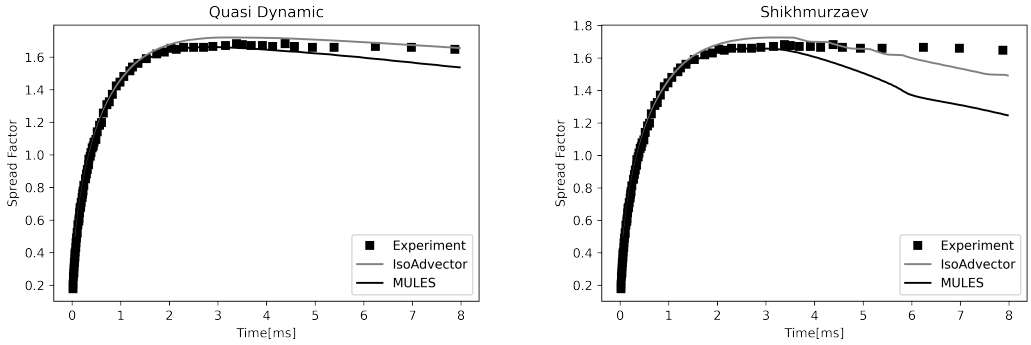

Quasi-Dynamic

Shikhmurzaev

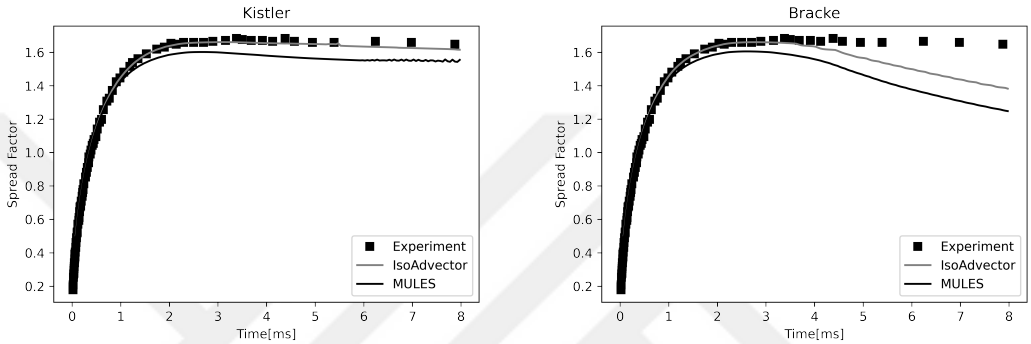

Kistler

Bracke

Figure 6.11 : Comparison of MULES and IsoAdvector in terms of spread factor for Case 3.

Table 6.4 : MSFE and MSDE of the simulations for Case 3.

Interface method	DCA Model	MSFE	MSDE
MULES	Shikhmurzaev	8.26%	-1.42%
MULES	Kistler	5.03%	-4.81%
MULES	Bracke	9.83%	-4.60%
MULES	Quasi-Dynamic	2.20%	-1.24%
IsoAdvector	Shikhmurzaev	3.46%	2.60%
IsoAdvector	Kistler	1.34%	-1.29%
IsoAdvector	Bracke	5.32%	-1.31%
IsoAdvector	Quasi-Dynamic	2.57%	2.24%

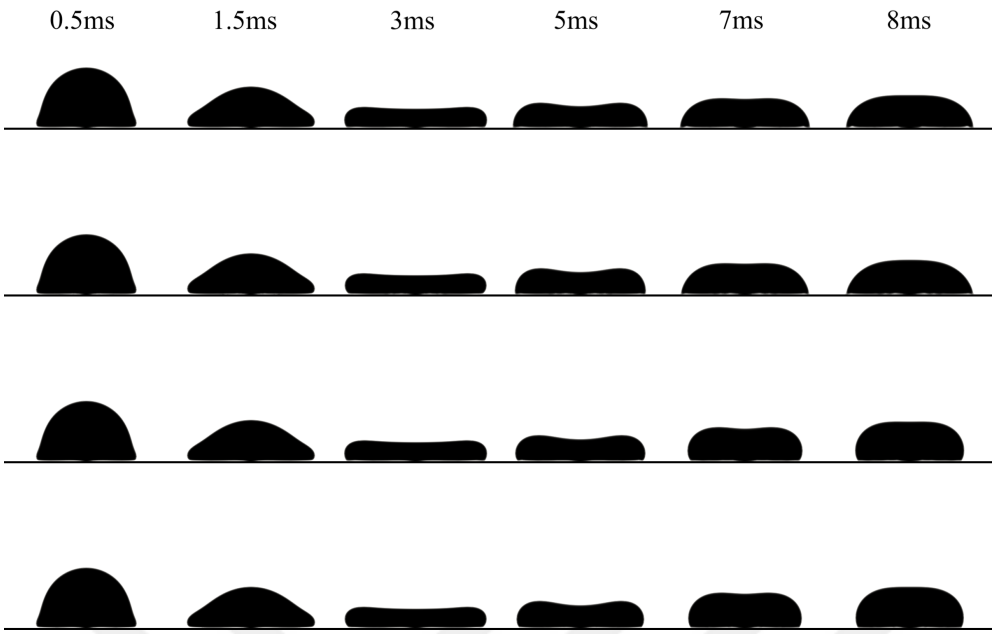

Figure 6.12 : Temporal evolution of the droplet shapes in MULES simulations for Case 3. DCA models from top to bottom: Quasi-Dynamic, Kistler, Shikhmurzaev and Bracke.

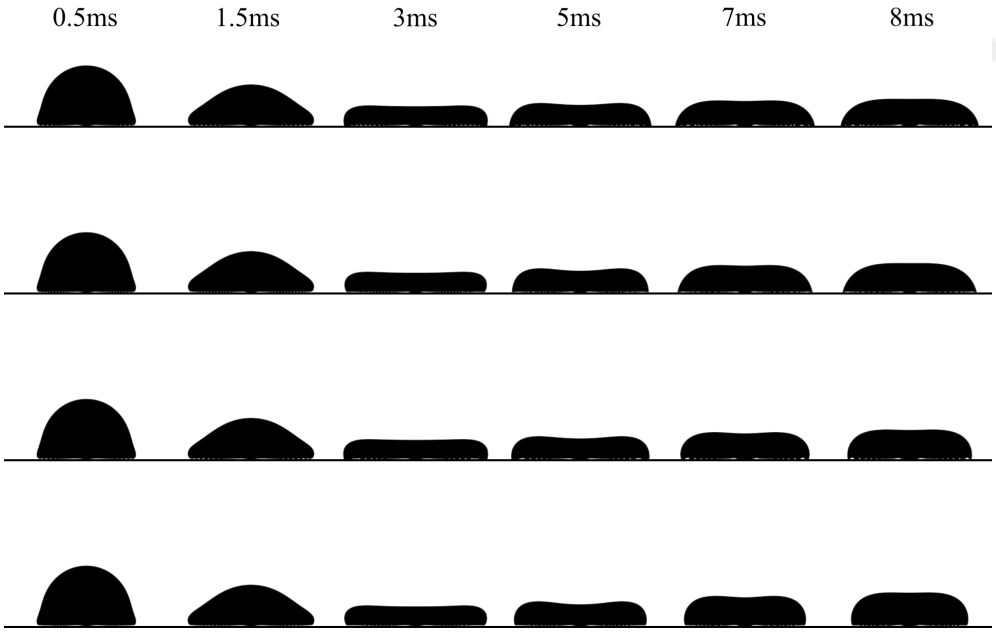

Figure 6.13 : Temporal evolution of the droplet shapes in IsoAdvector simulations for Case 3. DCA models from top to bottom: Quasi-Dynamic, Kistler, Shikhmurzaev and Bracke.

6.2.4 Case 4

This experiment is conducted by impinging a water droplet of 2.5 mm diameter onto a stainless steel surface with 0.48 m/s initial velocity. The contact angles are $\theta_A = 120^\circ$ and $\theta_R = 60^\circ$. The Reynolds and Weber numbers are 1200 and 7.9, respectively.

Due to the low Weber number, the effect of the surface tension is more dominant compared to the previous cases. Hence, the numerical calculations are much more affected by the problematic nature of the surface tension calculations, which is caused by the singularity in the contact line. One way to overcome this problem is to relax the no-slip boundary condition at the solid surface, and another is to use a diffuse interface. Since we want to test all the cases in the same setup, we didn't relax the no-slip boundary condition and, therefore, the IsoAdvector method which is not diffusive is not able to simulate this case and blows after a short time. Therefore, we can only show the results of the IsoAdvector simulations for the first 2.5 ms.

We can see that even though the IsoAdvector simulations only lasted for 2.5 ms, the droplet shapes are almost identical to the ones that are generated by the MULES simulations (See Figure 6.15). In the MULES simulations, the shapes of the droplets that are given by different DCA models are also similar (See Figure 6.16). All DCA models predict the spread diameter higher than the experiment. At around 7 ms, the models predict a recoiling behavior as can be seen in Figure 6.14, which is not present in the experiment. Despite all these, they yield close results and low errors (See Table 6.5). The Shikhmurzaev model has the lowest error in both the spread factor and the maximum spread diameter.

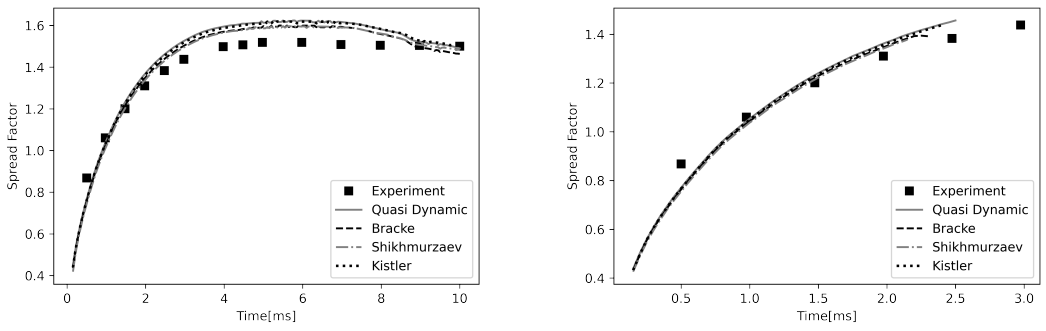

MULES IsoAdvector

Figure 6.14 : Comparison of DCA models in terms of spread factor for Case 4.

Table 6.5 : MSFE and MSDE of the simulations for Case 4.

Interface method	DCA Model	MSFE	MSDE
MULES	Shikhmurzaev	3.75%	5.11%
MULES	Kistler	4.88%	6.60%
MULES	Bracke	3.97%	5.31%
MULES	Quasi-Dynamic	5.03%	6.90%

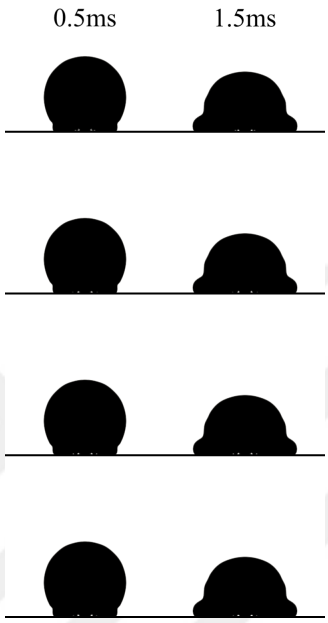

Figure 6.15 : Temporal evolution of the droplet shapes in IsoAdvector simulations for Case 4. DCA models from top to bottom Quasi-Dynamic, Kistler, Shikhmurzaev and Bracke.

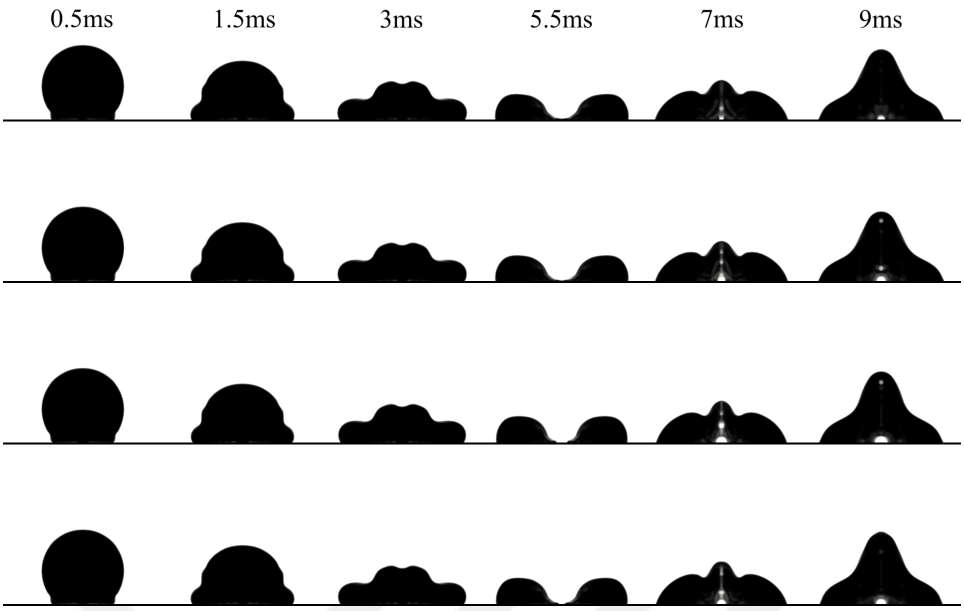

Figure 6.16 : Temporal evolution of the droplet shapes in MULES simulations for Case 4. DCA models from top to bottom Quasi-Dynamic, Kistler, Shikhmurzaev and Bracke.

6.2.5 Case 5

This experiment is conducted by impinging a water droplet of 2.5 mm diameter onto a stainless steel surface with 0.23 m/s initial velocity. The contact angles are $\theta_A = 120^\circ$ and $\theta_R = 60^\circ$. The Reynolds and Weber numbers are 575 and 1.81, respectively. This case has the lowest Weber number among the cases we have tested. So, the same situation regarding the IsoAdvector in Case 4 applies to this case as well.

Starting from 2.5 ms until the end of the simulation, the spread factor is always predicted lower than its actual values as shown in Figure 6.17. The small recoil starting from 10 ms followed by an increase in the spread factor are resolved but much larger in magnitudes. Also, the increase in the spread factor starts roughly 2.5 ms before it is observed in the experiments. The lowest errors are given by the Kistler model (See Table 6.6). The droplet shapes are given in Figure 6.18.

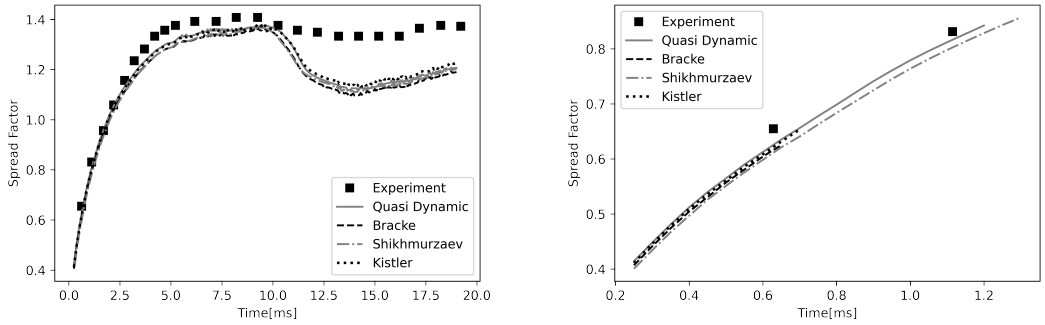

MULES IsoAdvector

Figure 6.17 : Comparison of DCA models in terms of spread factor for Case 5.

Table 6.6 : MSFE and MSDE of the simulations for Case 5.

Interface method	DCA Model	MSFE	MSDE
MULES	Shikhmurzaev	8.84%	-2.59%
MULES	Kistler	7.28%	-2.24%
MULES	Bracke	9.10%	-3.06%
MULES	Quasi-Dynamic	7.58%	-2.26%

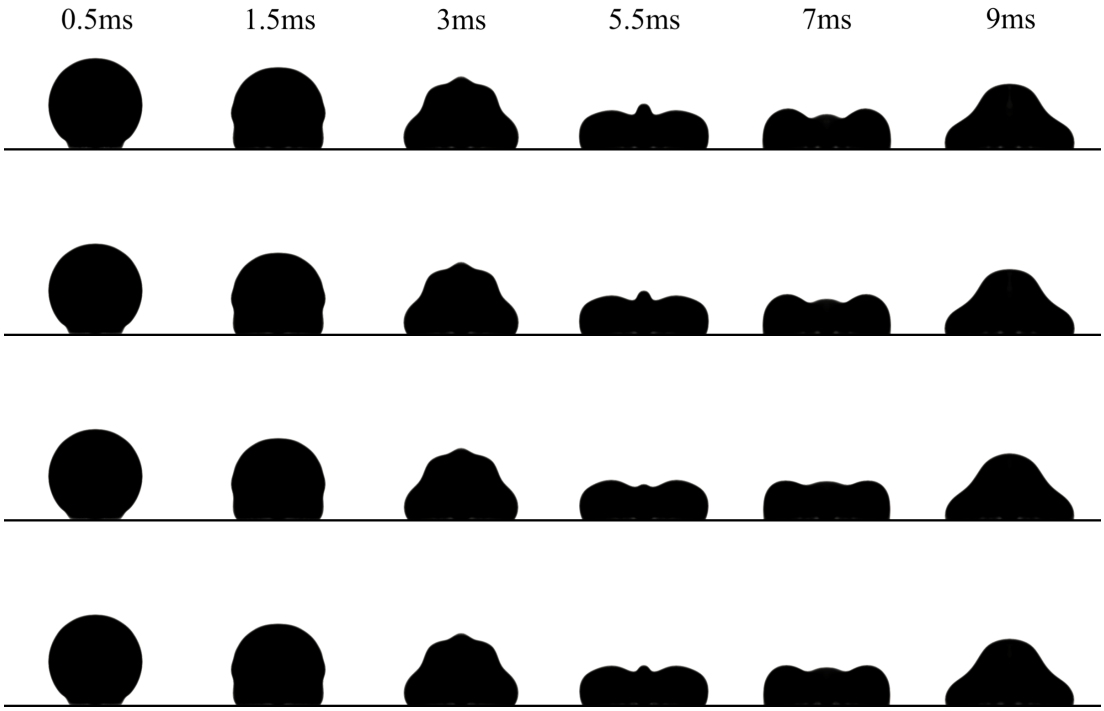

Figure 6.18 : Temporal evolution of the droplet shapes in MULES simulations for Case 5. DCA models from top to bottom Quasi-Dynamic, Kistler, Shikhmurzaev and Bracke.

7. CONCLUSIONS

In this study, numerical simulations of droplet impact on dry, smooth and solid surfaces were done using four different DCA models, namely the Quasi-Dynamic, the Kistler, the Bracke and the Shikhmurzaev models. These models are coupled with two VOF based interface capturing methods, which are the MULES and the IsoAdvector schemes. In order to compare the performances of the dynamic contact angle models and the interface capturing methods, five different physical experiments with different flow settings were simulated and the performances of the models were compared both qualitatively and quantitatively. For all simulations, we've drawn the droplet shapes at different time instances. The time instances were chosen so that the droplet shapes can be compared with the experiments. It is observed that the temporal evolution of the droplets matches with the physical experiments.

Even though we've discussed each experiment individually, we have discovered some patterns. Two of the five experiments had relatively low Reynolds numbers (36 and 575) compared to the other three (1200, 3245 and 4010). We have seen that for all experiments that have low Reynolds number, the maximum spread factor is estimated to be slightly lower than the experiments in 10 simulations out of 12. Similarly, all of the 20 simulations corresponding to the experiments with high Reynolds number slightly overestimates the maximum spread factor. Another pattern we've discovered is that, in all three experiments that have high Reynolds number, the Shikhmurzaev model has always yields the lowest errors in the spread factor and the maximum spread diameter both with the MULES and the IsoAdvector algorithms, whereas the experiments with low Reynolds number is best simulated with the Kistler model and the Quasi-Dynamic model.

Even though the sharp interface capturing methods such as the IsoAdvector method are generally not used with the no-slip boundary condition without workarounds because of the singularity at the contact line, we have shown that experiments with high Weber numbers can be simulated with the IsoAdvector algorithm, but the experiments with

low Weber numbers are failed to be simulated after 1 ms to 2 ms. Only considering the three experiments that we were able to run the IsoAdvector simulations, the experiments with high Weber numbers (90, 93) were predicted better in terms of the MSFE, whereas the experiment with moderate Weber number (52) was predicted better with the MULES algorithm. Of course, we cannot make robust conclusions using only three cases, therefore conducting more simulations with an increased number of cases which consists of a variety of Weber numbers is necessary for future work.

Overall, all contact angle models predict the temporal droplet spread factor evolution very well, the maximum obtained MSFE is 11.33% and the minimum obtained MSFE is 1.34% from all 32 simulations. In the majority of the simulations, the model that performs worst is the Quasi-Dynamic model, and the best performing model is the Shikhmurzaev model. However the difference between the Quasi-Dynamic model's performance and the Shikhmurzaev model's performance is very small. The same conclusions also apply to the performances for the maximum spread diameter prediction, with lowest MSDE being 1.24% and the highest being 11.31%. For all cases, the most accurate DCA models are summarized in Table 7.1

Table 7.1 : Most Accurate DCA Models.

Case	We	Re	Most Accurate DCA Model
Case 1	52	3245	Shikhmurzaev
Case 2	90	4010	Shikhmurzaev
Case 3	93	36	Quasi-Dynamic (MULES), Kistler (IsoAdvector)
Case 4	7.9	1200	Shikhmurzaev
Case 5	1.81	575	Kistler

REFERENCES

[1] **Luo, K.**, **Changxiao, S.**, **Min, C. and Fan, J.** (2019). Level set method for atomization and evaporation simulations, *Progress in Energy and Combustion Science*, *73*, 65–94.

[2] **Yokoi, K.**, **Vadillo, D.**, **Hinch, J. and Hutchings, I.** (2009). Numerical studies of the influence of the dynamic contact angle on a droplet impacting on a dry surface, *Physics of Fluids*, *21*(7), 072102.

[3] **Klitz, M.** (2015). *Numerical Simulation of Droplets with Dynamic Contact Angles*, (Doctoral dissertation). Retrieved from https://core.ac.uk/.

[4] **Gujjula, S.R.** (2016). *Numerical Investigation of Droplet Spread: Effect of Contact Angle Models*, (Master's thesis). Retrieved from https://etd.ohiolink.edu/.

[5] **Toda, K.** (2013). What Is Spray Coating?. In Automotive Painting Technology (pp. 5-43). Dordrecht : Springer.

[6] **Antonini, C.**, **Villa, F. and Marengo, M.** (2014). Oblique impacts of water drops onto hydrophobic and superhydrophobic surfaces: outcomes, timing, and rebound maps, *Experiments in Fluids*, *55*(4), 1713.

[7] **Sarkar, M.**, **Hasanuzzaman, M.**, **Gulshan, F. and Rashid, A.** (2020). Surface, Mechanical and Shape Memory Properties of Biodegradable Polymers and Their Applications, *Reference Module in Materials Science and Materials Engineering*.

[8] **Moldoveanu, S.C. and David, V.**, (2017). RP-HPLC Analytical Columns, *Selection of the HPLC Method in Chemical Analysis* (pp.279–328), Boston : Elsevier.

[9] **Law, K.Y.** (2014). Definitions for Hydrophilicity, Hydrophobicity, and Superhydrophobicity: Getting the Basics Right, *The Journal of Physical Chemistry Letters*, *5*(4), 686–688.

[10] **Rønneberg, S.**, **Xiao, S.**, **He, J. and Zhang, Z.** (2020). Nanoscale Correlations of Ice Adhesion Strength and Water Contact Angle, *Coatings*, *10*(4), 379.

[11] **Fukai, J.**, **Shiiba, Y.**, **Yamamoto, T. and Miyatake, O.** (1995). Wetting effects on the spreading of a liquid droplet colliding with a flat surface: Experiment and modeling, *Phys. Fluids*, *7*(2), 13.

[12] **Zhang, M.Y.**, **Zhang, H. and Zheng, L.L.** (2008). Simulation of droplet spreading, splashing and solidification using smoothed particle hydrodynamics method, *International Journal of Heat and Mass Transfer*, *51*(13), 3410–3419.

[13] **Shen, S.**, **Bi, F. and Guo, Y.** (2012). Simulation of droplets impact on curved surfaces with lattice Boltzmann method, *International Journal of Heat and Mass Transfer*, *55*(23), 6938–6943.

[14] **Frank, X. and Perré, P.** (2012). Droplet spreading on a porous surface: A lattice Boltzmann study, *Physics of Fluids*, *24*(4), 042101.

[15] **Kearney, R.V. and Bewley, G.P.** (2020). Lagrangian tracking of colliding droplets, *Experiments in Fluids*, *61*(7), 155.

[16] **Shigorina, E.**, **Kordilla, J. and Tartakovsky, A.M.** (2017). Smoothed particle hydrodynamics study of the roughness effect on contact angle and droplet flow, *Physical Review E*, *96*(3), 033115.

[17] **Fujimoto, H.**, **Shiotani, Y.**, **Tong, A.Y.**, **Hama, T. and Takuda, H.** (2007). Three-dimensional numerical analysis of the deformation behavior of droplets impinging onto a solid substrate, *International Journal of Multiphase Flow*, *33*(3), 317–332.

[18] **Jiang, M.**, **Zhou, B. and Wang, X.** (2018). Comparisons and validations of contact angle models, *International Journal of Hydrogen Energy*, *43*(12), 6364–6378.

[19] **Joshi, A.**, **Khalasi, K. and Banerjee, J.** (2019). Evaluation of Droplet Spread on Surface Using Dynamic Contact Angle Model, *ICTEA: International Conference on Thermal Engineering*, Ghandinagar, Gujarat, India, February 23-26.

[20] **Sun, J.**, **Liu, Q.**, **Liang, Y.**, **Lin, Z. and Liu, C.** (2019). Three-dimensional VOF simulation of droplet impacting on a superhydrophobic surface, *Bio-Design and Manufacturing*, *2*(1), 10–23.

[21] **Malgarinos, I.**, **Nikolopoulos, N.**, **Marengo, M.**, **Antonini, C. and Gavaises, M.** (2014). VOF simulations of the contact angle dynamics during the drop spreading: Standard models and a new wetting force model, *Advances in Colloid and Interface Science*, *212*, 1–20.

[22] **Pasandideh-Fard, M.**, **Bhola, R.**, **Chandra, S. and Mostaghimi, J.** (1998). Deposition of tin droplets on a steel plate: simulations and experiments, *International Journal of Heat and Mass Transfer*, *41*(19), 2929–2945.

[23] **Gunjal, P.R.**, **Ranade, V.V. and Chaudhari, R.V.** (2005). Dynamics of drop impact on solid surface: Experiments and VOF simulations, *AIChE Journal*, *51*(1), 59–78.

[24] **Griebel, M. and Klitz, M.**, (2014). Simulation of droplet impact with dynamic contact angle boundary conditions. In *Singular Phenomena and Scaling inMathematical Models* (pp.297–325), Cham : Springer.

[25] **Caviezel, D.**, **Narayanan, C. and Lakehal, D.** (2008). Adherence and bouncing of liquid droplets impacting on dry surfaces, *Microfluidics and Nanofluidics*, *5*(4), 469–478.

[26] **Emdadi, M. and Pournaderi, P.** (2019). Study of droplet impact on a wall using a sharp interface method and different contact line models, *Journal of Applied Fluid Mechanics*, *12*(4), 1001–1012.

[27] **Pendota, P.** (2015). *Numerical Simulation of Dynamic Contact Angles and Contact Lines in Multiphase Flows using Level Set Method*, (Master's thesis). Retrieved from https://core.ac.uk/.

[28] **Šikalo, Š.**, **Wilhelm, H.D.**, **Roisman, I.V.**, **Jakirlić, S. and Tropea, C.** (2005). Dynamic contact angle of spreading droplets: Experiments and simulations, *Physics of Fluids*, *17*(6), 062103.

[29] **Shin, S. and Juric, D.** (2009). Simulation of droplet impact on a solid surface using the level contour reconstruction method, *Journal of Mechanical Science and Technology*, *23*(9), 2434–2443.

[30] **Harlow, F.H. and Shannon, J.P.** (1967). The Splash of a Liquid Drop, *Journal of Applied Physics*, *38*(10), 3855–3866.

[31] **Tsurutani, K.**, **Yao, M.**, **Senda, J. and Fujimoto, H.** (1990). Numerical Analysis of the Deformation Process of a Droplet Impinging upon a Wall, *JSME international journal. Ser. 2, Fluids engineering, heat transfer, power, combustion, thermophysical properties*, *33*(3), 555–561.

[32] **Kistler, S.F.,** (1993). Hydrodynamics of Wetting. In *Wettability* (pp. 311-430), New York : CRC Press.

[33] **Jiang, T.S.**, **Soo-Gun, O. and Slattery, J.C.** (1979). Correlation for dynamic contact angle, *Journal of Colloid and Interface Science*, *69*(1), 74–77.

[34] **Shikhmurzaev, Y.D.** (2007). *Capillary Flows with Forming Interfaces*, New York : Chapman and Hall/CRC.

[35] **Blake, T.D.** (2006). The physics of moving wetting lines, *Journal of Colloid and Interface Science*, *299*(1), 1–13.

[36] **Bracke, M.**, **Voeght, F. and Joos, P.**, (1989). The kinetics of wetting: the dynamic contact angle, *Trends in Colloid and Interface Science III*, 142–149.

[37] **Sabisch, W.** (2000). *Dreidimensionale numerische Simulation der Dynamik von aufsteigenden Einzelblasen und Blasenschwärmen mit einer Volume-of-Fluid-Methode*, (Doctoral dissertation). Retrieved from https://publikationen.bibliothek.kit.edu/.

[38] **Graveleau, M. and Tchelepi, H.** (2016). *Pore-scale simulation of mass transfer across immiscible interfaces*, (Master's thesis). Retrieved from https://pangea.stanford.edu/.

[39] **Whitaker, S.** (2013). *The method of volume averaging* (Vol. 13), Dordrecht : Springer Science & Business Media.

[40] **Hirt, C.W. and Nichols, B.D.** (1981). Volume of fluid (VOF) method for the dynamics of free boundaries, *Journal of Computational Physics*, *39*(1), 201–225.

[41] **Young, T.** (1805). III. An essay on the cohesion of fluids, *Philosophical Transactions of the Royal Society of London*, *95*, 65–87.

[42] **Yuan, Y. and Lee, T.R.**, (2013). Contact Angle and Wetting Properties. In *SurfaceScience Techniques* (pp.3-34), Berlin : Springer.

[43] **Krumpfer, J.W. and McCarthy, T.J.** (2010). Contact angle hysteresis: a different view and a trivial recipe for low hysteresis hydrophobic surfaces, *Faraday Discussions*, *146*(0), 103–111.

[44] **Eral, H.B.**, **Mannetje, D.J.C.M.'t and Oh, J.M.** (2013). Contact angle hysteresis: a review of fundamentals and applications, *Colloid and Polymer Science*, *291*(2), 247–260.

[45] **Hoffman, R.L.** (1975). A study of the advancing interface. I. Interface shape in liquid—gas systems, *Journal of Colloid and Interface Science*, *50*(2), 228–241.

[46] **Göhl, J.**, **Mark, A.**, **Sasic, S. and Edelvik, F.** (2018). An immersed boundary based dynamic contact angle framework for handling complex surfaces of mixed wettabilities, *International Journal of Multiphase Flow*, *109*, 164–177.

[47] **Popescu, M.N.**, **Ralston, J. and Sedev, R.** (2008). Capillary Rise with Velocity-Dependent Dynamic Contact Angle, *Langmuir*, *24*(21), 12710–12716.

[48] **Andersson, M.**, **Vukčević, V.**, **Zhang, S.**, **Qi, Y.**, **Jasak, H.**, **Beale, S.B. and Lehnert, W.** (2019). Modeling of droplet detachment using dynamic contact angles in polymer electrolyte fuel cell gas channels, *International Journal of Hydrogen Energy*, *44*(21), 11088–11096.

[49] **Nichita, B.A.**, **Zun, I. and Thome, J.R.** (2010). A VOF method coupled with a dynamic contact angle model for simulation of two-phase flows with partial wetting, *7th International Conference on Multiphase Flow, ICMF*, Tampa, FL, May 30–June 4.

[50] **Rioboo, R.**, **Marengo, M. and Tropea, C.** (2002). Time evolution of liquid drop impact onto solid, dry surfaces, *Experiments in Fluids*, *33*(1), 112–124.

[51] **Šikalo, Š.**, **Wilhelm, H.D.**, **Roisman, I.V.**, **Jakirlić, S. and Tropea, C.** (2005). Dynamic contact angle of spreading droplets: Experiments and simulations, *Physics of Fluids*, *17*(6), 062103.

[52] **Roisman, I.**, **Opfer, L.**, **Tropea, C.**, **Raessi, M.**, **Mostaghimi, J. and Chandra, S.** (2008). Drop impact onto a dry surface: Role of the dynamic contact angle, *Colloids and Surfaces A: Physicochemical and Engineering Aspects*, *322*(1-3), 183–191.

[53] **OpenFOAM | Free CFD Software | The OpenFOAM Foundation.** (2021). *Retrieved September 21, 2021, from https://openfoam.org/*

[54] **Roenby, J.**, **Bredmose, H. and Jasak, H.** (2016). A computational method for sharp interface advection, *Royal Society Open Science*, *3*(11), 160405.

[55] **Deshpande, S.S.**, **Anumolu, L. and Trujillo, M.F.** (2012). Evaluating the performance of the two-phase flow solver interFoam, *Computational Science & Discovery*, *5*(1), 014016.

[56] **Larsen, B.E.**, **Fuhrman, D.R. and Roenby, J.** (2019). Performance of interFoam on the simulation of progressive waves, *Coastal Engineering Journal*, *61*(3), 380–400.

[57] **Aarnikoivu, R.** *et al.* (2021). *An investigation on using the volume of fluid method to study the bubble sweep-down phenomenon in marine context*,(Master's thesis). Retrieved from https://aaltodoc.aalto.fi/.

[58] **Brackbill, J.**, **Kothe, D. and Zemach, C.** (1992). A continuum method for modeling surface tension, *Journal of Computational Physics*, *100*(2), 335–354.

APPENDICES

APPENDIX A.1 : fvSchemes and fvSolutions files used in IsoAdvector simulations
APPENDIX A.2 : fvSchemes and fvSolutions files used in MULES simulations

APPENDIX A.1

fvSchemes dictionary used with IsoAdvector simulations is as follows:

```
FoamFile
{
    version     2.0;
    format      ascii;
    class       dictionary;
    location    "system";
    object      fvSchemes;
}

ddtSchemes
{
    default         CrankNicolson 0.5;
}

gradSchemes
{
    default         Gauss linear;
}

divSchemes
{
    div(rhoPhi,U)  Gauss upwind;
    div(phi,alpha)  Gauss vanLeer;
    div(phirb,alpha) Gauss interfaceCompression;
    div(((rho*nuEff)*dev2(T(grad(U))))) Gauss linear;
}

laplacianSchemes
{
    default         Gauss linear corrected;
}

interpolationSchemes
{
    default         linear;
}

snGradSchemes
{
```

```
    default         corrected;
}

fluxRequired
{
    default         no;
    p_rgh;
    pcorr;
    alpha.water;
}
```

fvSolutions dictionary used with IsoAdvector simulations is as follows:

```
 FoamFile
{
    version     2.0;
    format      ascii;
    class       dictionary;
    location    "system";
    object      fvSolution;
}

solvers
{
    "alpha.water.*"
    {
        interfaceMethod "isoAdvector";
        isoFaceTol      1e-8;
        surfCellTol     1e-8;
        snapTol         1e-12;
        nAlphaBounds    3;
        clip            true;


        nAlphaCorr      2;
        nAlphaSubCycles 1;
        cAlpha          1;

        MULESCorr       yes;
        nLimiterIter    8;

        solver          smoothSolver;
        smoother        symGaussSeidel;
        tolerance       1e-8;
        relTol          0;
    }
```

```
"pcorr.*"
{
    solver          PCG;
    preconditioner  DIC;
    tolerance       1e-10;
    relTol          0;
}

"p_rgh"
{
    solver          GAMG;
    tolerance       1e-8;
    relTol          1e-3;
    smoother        DIC;
    nPreSweeps      0;
    nPostSweeps     2;
    nFinestSweeps   2;
    cacheAgglomeration true;
    nCellsInCoarsestLevel 10;
    agglomerator    faceAreaPair;
    mergeLevel      1;
}

"p_rghFinal"
{
    solver          PCG;
    preconditioner
    {
        preconditioner  GAMG;
        tolerance       1e-8;
        relTol          0;
        nVcycles        2;
        smoother        DICGaussSeidel;
        nPreSweeps      2;
        nPostSweeps     2;
        nFinestSweeps   2;
        cacheAgglomeration true;
        nCellsInCoarsestLevel 10;
        agglomerator    faceAreaPair;
        mergeLevel      1;
    }
    tolerance       1e-9;
    relTol          0;
    maxIter         50;
}
U
{
    solver          smoothSolver;
```

```
        smoother        DILUGaussSeidel;
        tolerance       1e-7;
        relTol          0.05;
        nSweeps         5;
        minIter         3;
    }

    UFinal
    {
        solver          smoothSolver;
        smoother        GaussSeidel;
        tolerance       1e-8;
        relTol          0;
        nSweeps         2;
    }


}

PIMPLE
{
    momentumPredictor yes;
    nCorrectors       3;
    nOuterCorrectors  1;
    nNonOrthogonalCorrectors 0;
    nAlphaCorr        1;
    nAlphaSubCycles   1;
    cAlpha            1;
}
```

APPENDIX A.2

fvSchemes dictionary used with MULES simulations is as follows:

```
FoamFile
{
    version     2.0;
    format      ascii;
    class       dictionary;
    location    "system";
    object      fvSchemes;
}

ddtSchemes
```

```
{
    default         CrankNicolson 0.5;
}

gradSchemes
{
    default         leastSquares;
}

divSchemes
{
    div(rhoPhi,U)  Gauss limitedLinearV 0.5;
    div(phi,alpha)  Gauss vanLeer;
    div(phirb,alpha) Gauss interfaceCompression;
    div(((rho*nuEff)*dev2(T(grad(U))))) Gauss linear;
}

laplacianSchemes
{
    default         Gauss linear corrected;
}

interpolationSchemes
{
    default         linear;
}

snGradSchemes
{
    default         corrected;
}

fluxRequired
{
    default         no;
    p_rgh;
    pcorr;
    alpha.water;
}
```

fvSolutions dictionary used with MULES simulations is as follows:

```
 FoamFile
{
    version     2.0;
    format      ascii;
```

```
    class       dictionary;
    location    "system";
    object      fvSolution;
}

solvers
{
    "alpha.water.*"
    {
        nAlphaCorr      2;
        nAlphaSubCycles 1;
        cAlpha          0.3;

        MULESCorr       yes;
        nLimiterIter    8;

        solver          smoothSolver;
        smoother        symGaussSeidel;
        tolerance       1e-8;
        relTol          0;
    }

    "pcorr.*"
    {
        solver          PCG;
        preconditioner  DIC;
        tolerance       1e-10;
        relTol          0;
    }

    "p_rgh"
    {
        solver          GAMG;
        tolerance       1e-8;
        relTol          1e-3;
        smoother        DIC;
        nPreSweeps      0;
        nPostSweeps     2;
        nFinestSweeps   2;
        cacheAgglomeration true;
        nCellsInCoarsestLevel 10;
        agglomerator    faceAreaPair;
        mergeLevel      1;
    }

    "p_rghFinal"
    {
        solver          PCG;
```

```
        preconditioner
        {
            preconditioner  GAMG;
            tolerance       1e-8;
            relTol          0;
            nVcycles        2;
            smoother        DICGaussSeidel;
            nPreSweeps      2;
            nPostSweeps     2;
            nFinestSweeps   2;
            cacheAgglomeration true;
            nCellsInCoarsestLevel 10;
            agglomerator    faceAreaPair;
            mergeLevel      1;
        }
        tolerance       1e-9;
        relTol          0;
        maxIter         50;
    }
    U
    {
        solver          smoothSolver;
        smoother        DILUGaussSeidel;
        tolerance       1e-7;
        relTol          0.05;
        nSweeps         5;
        minIter         3;
    }

    UFinal
    {
        solver          smoothSolver;
        smoother        GaussSeidel;
        tolerance       1e-8;
        relTol          0;
        nSweeps         2;
    }


}

PIMPLE
{
    momentumPredictor yes;
    nCorrectors       3;
    nOuterCcorrectors  1;
    nNonOrthogonalCorrectors 0;
    nAlphaCorr        1;
```

```
    nAlphaSubCycles   1;
    cAlpha            1;
}
```

CURRICULUM VITAE

Name Surname : Tahir Tekin Filiz

EDUCATION :

- **B.Sc.** : 2016, Yıldız Technical University, Faculty of Mechanical Engineering, Department of Mechanical Engineering